Biomechanics and Modeling in Mechanobiology (2019) 18:1529–1548
https://doi.org/10.1007/s10237-019-01163-z

ORIGINAL PAPER

CardioFAN: open source platform for noninvasive assessment of pulse transit time and pulsatile flow in hyperelastic vascular networks

Yashar Seyed Vahedein[1] · **Alexander S Liberson**[1]

Received: 9 December 2018 / Accepted: 26 April 2019 / Published online: 10 May 2019

Abstract
A profound analysis of pressure and flow wave propagation in cardiovascular systems is the key in noninvasive assessment of hemodynamic parameters. Pulse transit time (PTT), which closely relates to the physical properties of the cardiovascular system, can be linked to variations of blood pressure and stroke volume to provide information for patient-specific clinical diagnostics. In this work, we present mathematical and numerical tools, capable of accurately predicting the PTT, local pulse wave velocity, vessel compliance, and pressure/flow waveforms, in a viscous hyperelastic cardiovascular network. A new one-dimensional framework, entitled cardiovascular flow analysis (CardioFAN), is presented to describe the pulsatile fluid–structure interaction in the hyperelastic arteries, where pertaining hyperbolic equations are solved using a high-resolution total variation diminishing Lax–Wendroff method. The computational algorithm is validated against well-known numerical, *in vitro* and *in vivo* data for networks of main human arteries with 55, 37 and 26 segments, respectively. PTT prediction is improved by accounting for hyperelastic nonlinear waves between two arbitrary sections of the arterial tree. Consequently, arterial compliance assignments at each segment are improved in a personalized model of the human aorta and supra-aortic branches with 26 segments, where prior in vivo data were available for comparison. This resulted in a 1.5% improvement in overall predictions of the waveforms, or average relative errors of 5.5% in predicting flow, luminal area and pressure waveforms compared to prior *in vivo* measurements. The open source software, CardioFAN, can be calibrated for arbitrary patient-specific vascular networks to conduct noninvasive diagnostics.

Keywords Subject-specific hemodynamics modeling · Hyperelastic constitutive model · Fluid–structure interaction (FSI) · Compliance discontinuity · Pulse transit time (PTT) · Nonlinear wave propagation

1 Introduction

Clinical experiments (*i.e., in vivo*) and experimental (*i.e., in vitro*) models of the cardiovascular systems initiated significant improvement in diagnostic capabilities, stimulating development of the fields such as biomedical engineering and biomechanics (Bronzino 2005). Followed by computational simulations, the first numerical model of an artery in the cardiovascular system which accounted for the distensibility of the arteries was developed by (Perktold et al. 1991). More sophisticated models followed (Alastruey 2006; Sherwin et al. 2003b; Formaggia et al. 2003; Dong et al. 2006; Figueroa et al. 2009) which enhanced our understanding of the mechanism of blood flow and pulse propagation in cardiovascular system. With technological advancements, current computational models are becoming significantly more promising for the future of surgical planning, and for studying/monitoring cardiovascular health (van Bakel et al. 2018; Gray and Pathmanathan 2018). Appearance of FDA-cleared devices such as (Heartflow Ⓡ FFRCT and the Medtronic CardioInsightⓇ Cardiac Mapping System) and the addition of new FDA regulations (Gray and Pathmanathan 2018) are more supporting evidence that the computational methods are now producing clinically viable results.

Computational models can noninvasively capture the mechanistic behavior in a studied region of the cardiovascular system. When calibrated, these models can provide patient-specific data using pulsatile blood flow properties. Validated computational models have a significant advantage

✉ Yashar Seyed Vahedein
Yashar.Seyed.Vahedein@rit.edu

Alexander S Liberson
asleme@rit.edu

[1] Rochester Institute of Technology, 76 Lomb Memorial Drive, Rochester, NY 14623, USA

over invasive, costly and time-consuming experimental models and clinical tests. However, they require clinical measurements for calibration and evaluation of the patient-specific data (Itu et al. 2017). Alternatively, the data collected from computational models can be combined with experimental/clinical measurements to improve diagnostics capabilities of the current devices (*Data Assimilation* (Veneziani and Vergara 2013)).

Cardiovascular disorders and medical interventions can be diagnosed by quantification and monitoring distributions of the cardiac output, blood pressure, blood flow, pulse wave velocity (PWV) and arterial compliance along the aorta or any of the large arteries of interest (Nichols and Edwards 2001). In addition, the arterial wall stiffness, which governs the distensibility of arterial walls, along with the wave reflections at the peripheral vascular bed have been clinically identified as the primary biomarkers of the pulse wave propagation and cardiovascular health (Mitchell 2009). In recent years, extensive work has been done on measuring wave reflections and PWV (Tavallali et al. 2018), or its surrogate pulse transit time (PTT) (Djelić et al. 2013; Pereira et al. 2015). The relation between PWV(or PTT) and cardiovascular diseases, such as a reduction in PTT as an indicator of hypertension (García et al. 2014; Liang et al. 2018), among others (Foo and Lim 2006; Sharwood-Smith et al. 2006), have been previously studied. This has made the accurate prediction of pulse wave propagation an indispensable part of the recent cardiovascular simulations (Poleszczuk et al. 2018).

New advances in the computer power have provided researchers with the ability to model large-scale 1D and 3D models (Shi et al. 2011; Humphrey 1995). In contrast to local 3D geometrically accurate models, reduced-order models are not yet widely available as the diagnostic means for physicians. These models are usually validated against in vitro data (Anliker et al. 1970; Westerhof et al. 1971), since a physiologically accurate data calibration and validation is required to overcome the natural noise in the cardiovascular system (Veneziani and Vergara 2013). Global 1D models introduce acceptable accuracy in capturing the physiological mechanisms of blood hemodynamics while having a marginally faster convergence rate compared to 3D models. Their application is justified by the long-wave approximation, making them ideal to be coupled with a local 3D model of a confined area of interest (van de Vosse and Stergiopulos 2011) or lumped parameter (0D) models replacing the outlet to the rest of a cardiovascular network.

The majority of theoretical models developed to describe the fluid–structure interaction (FSI) in the vascular circulatory system use linear elastic or viscoelastic constitutive equations for the wall coupled with the one-dimensional averaged momentum equation for the fluid. However, the stress–strain relationship for biological tissue is essentially nonlinear (Fung et al. 1979). Fung et al. introduced an anisotropic model, which accounts for the directionality of the elastic properties. The model constants can be calibrated by measuring the pressure and diameter of the main arteries with clinical or experimental measurements. (Humphrey and Taylor 2008) mentioned that the physical nonlinearity is crucial for an accurate prediction of pulsatile blood flow properties in case of studying an aortic aneurism. It was proven by (Liberson et al. 2016) that the match of measured and estimated values of PWV can be only obtained when the hyperelasticity of arterial wall is introduced.

To the knowledge of authors, the current numerical algorithms applied to the 1D (reduced order) models do not necessarily preserve the monotonic property. Monotonicity preserving (i.e., high resolution) schemes can retain the shape of waveform without creating artificial oscillations (Harten 1983). This approach may not cause a significant difference when a smooth solution exists, such as for pressure or flow waveforms in healthy patients or when studying hypertension (Segers et al. 2007). However, in case of a discontinuity in the properties, *e.g.,* stented or prosthetic artery (Kolodgie et al. 2007), the only class of solvers that can provide a solution without simplistic smoothing of the waveforms (Formaggia et al. 2003) is the monotonicity preserving solvers. Monotonicity preserving or total variation diminishing (TVD) schemes can also be used for continuous monitoring/prediction of cardiovascular health due to the discontinuous nature of cardiovascular events. These numerical schemes are free of dispersion caused by approximating the odd derivatives in the Taylor expansion of the governing partial differential equations (PDEs), making them ideal for resolving discontinuous properties.

The general approach of Hamilton's variational principle is utilized here to construct a unique form of the FSI equations governing the blood flow in the arterial system. The quasi-1D-reduced FSI model is simple to execute and alter, can be coupled to geometrically multiscale simulations (Vahedein and Liberson 2017; Vahedein et al. 2018) and provides quick solutions for the hyperbolic PDEs governing the nonlinear pulsatile flow in an arbitrary arterial network. The utilized approach demonstrates an improvement in accuracy due to the account of hyperelastic wall properties, along with the employment of a high-resolution monotone numerical scheme. The created software, named CardioFAN (Cardiovascular Flow Analysis), is validated against available data from numerical, in vitro and in vivo experiments for networks of arteries with 55, 37 and 26 main arterial segments (Alastruey 2006; Matthys et al. 2007; Alastruey et al. 2011, 2012, 2016), respectively. The effect of physical nonlinearity on the correct calculation of the PTT, pressure, flow and luminal vessel area is displayed. The physics-based nonlinear constitutive framework can be adequately tested, calibrated and applied for patient-specific clinical diagnosis and

prediction. We present the algorithm for calculating numerical PTT for hyperelastic arteries, sensitive to variation of the blood pressure and the stroke volume. This PTT calculation technique can also complement the studies investigating the feasibility of tracking variations of cardiovascular markers by measurements of the PTT or PWV (Carek et al. 2017; Mukkamala et al. 2015). The new method is used here to improve the calculation of the speed of wave propagation based on the prior in vivo data provided by (Alastruey et al. 2016). Compared to prior numerical simulations of this data, CardioFAN improved the flow, luminal area and pressure waveform predictions by 1.5%, with averaged relative errors smaller than 5.5% between simulated and *in vivo* waveforms. As shown in Sect. 3.3, with the current method, assigning a uniform or nonuniform speed of propagation values as the input properties of each segment, leads to improved waveform predictions. CardioFAN is now available for free and can be accessed from the provided links. Reliability test of this code conducted here is an important step toward preparing it for noninvasive and patient-specific diagnostics and data assimilation (Veneziani and Vergara 2013) purposes.

2 Methods

2.1 Blood properties

Although blood rheology is proved to be non-Newtonian (Pries et al. 1992), previous studies have shown that the blood viscosity model does not significantly affect the PWV when simulating large human arteries (Parkhurst et al. 2012; Caro et al. 2011). According to (Sankar and Hemalatha 2007), non-Newtonian fluid model is only required for small arteries with diameters $D < 100\ \mu m$, where the shear rate reduces to less than $1\ s^{-1}$. Therefore, for the larger arteries, we can use the Newtonian flow assumption. On the other hand, 90% of the blood consists of water (Caro et al. 2011), and since the suspended materials are several orders of magnitudes smaller than arterial diameter, the blood can be considered homogeneous and incompressible with a density of $\rho_f = 1050\ kg/m^3$ and viscosity of $\mu = 4.0\ mPa.s$ (Caro et al. 2011) (used in 55 segment case, Sect. 3.1). We used $\rho_f = 1050\ kg/m^3$, $\mu = 2.0\ mPa.s$ and $\rho_f = 1060\ kg/m^3$, $\mu = 3.5\ mPa.s$ for the *in vitro* (Matthys et al. 2007) and *in vivo* (Alastruey et al. 2016) validation cases, respectively.

2.2 Governing equations

Reduced mathematical model for cardiovascular networks results in a hyperbolic set of partial differential equations, describing interaction of an incompressible blood fluid motion with a viscous hyperelastic vessel wall. The averaging across the section of a flow path is based on the Hamilton's variational principle governing the process of a fluid–structure interaction (Liberson et al. 2017)

$$\begin{aligned}\delta I =& \delta I_{fluid} + \delta I_{solid} = \\ =& \int_{t_1}^{t_2} \left[\oint_{\forall_{\text{fluid(t)},}} \rho_f \delta L_f d\forall + \oint_{\forall_{\text{solid(t)},}} \delta L_s d\forall \right] dt = 0 \end{aligned} \tag{1}$$

Here, δI_{fluid} ,δI_{solid} are the variations of action components across fluid and solid volumes $\forall_{fluid(t)}$, $\forall_{solid(t)}$; t – time, ρ_f density of the fluid, L_f, L_s - the Lagrangian density functions for fluid and solids, respectively.

2.2.1 Fluid domain

As it is mentioned by (Berdichevsky 2009), variation of the Lagrange function density in Eulerian coordinates can be written as follows:

$$\delta L_f = \delta \left(\frac{\boldsymbol{V}^2}{2} - U(\rho_f, S, \nabla \boldsymbol{u}) \right) + T\delta S \tag{2}$$

where $\boldsymbol{V}$ – is a velocity vector, U – is an internal energy as a function of density, S – entropy, $\nabla \boldsymbol{u}$ (gradient of a displacement vector $\boldsymbol{u}$) - a distortion tensor and T – is temperature. The variation of the function must vanish for any admissible variations $\delta \boldsymbol{u}$ The derivation of fluid flow equations based on the Hamilton's variational principle is previously shown in detail (Liberson et al. 2017). Here, the effect of gravity force is added to the reduced momentum equation which affects the circulation when patient is in standing upright position

$$\begin{aligned} &\frac{\partial \overline{V}}{\partial t} + \frac{\partial}{\partial x}\left(a_1 \frac{P}{\rho_f} + a_2 \overline{V}^2 \right) \\ &\quad = \frac{1}{a_0 \rho}\left[\int rf(\mathrm{r})\, \sigma(\mathrm{x,r,t}) dr - R\, \tau(\mathrm{x,R,t}) \right] + g_\tau \\ &a_0 = \int rf(\mathrm{r}) dr; \\ &a_1 = \int r\varphi(\mathrm{r}) f(\mathrm{r}) dr; \\ &a_2 = \frac{1}{a_0} \int r\varphi(\mathrm{r})^2 f(\mathrm{r}) dr \end{aligned} \tag{3}$$

where g_τ is a gravitational acceleration in the direction of the streamline, $f(\mathrm{r})$, $\varphi(\mathrm{r})$- the specified function distributions of axial velocity and displacement accordingly, r – radial coordinate, R- internal wall radius P – blood pressure, $\overline{V}$ – averaged across the flow path section fluid velocity, $\boldsymbol{\sigma}$, $\boldsymbol{\tau}$ are the axial deviatoric and shear stress tensor components accordingly.

(Schultz et al. 2008) showed that velocity profile is mostly flat in large arteries, unlike peripheral arteries where profile

is close to the parabolic shape (Olufsen et al. 2000). In case of Newtonian fluid ($\sigma = 2\rho_f \nu \frac{\partial V}{\partial x}$, $\tau = \rho_f \nu \frac{\partial V}{\partial r}$, ν – kinematic viscosity), by utilizing the generalized Hagen-Poiseuille velocity profile $\varphi(r) = \frac{\gamma+2}{\gamma}\left[1 - \left(\frac{r}{R}\right)^{\gamma}\right]$ and a constant profile for the displacement distribution $f\ (r) = 1$, Eq. (3) takes the form presented in (Peiró and Veneziani 2009)

$$\frac{\partial \overline{V}}{\partial t} + \frac{\partial}{\partial x}\left(\alpha \frac{\overline{V}^2}{2} + \frac{P}{\rho_f}\right) = \nu\left(\frac{\partial^2 \overline{V}}{\partial x^2} - 2(\gamma+2)\frac{\overline{V}}{R^2}\right) + g_\tau \tag{4}$$

Momentum Eq. (4) is complemented by an averaged over the cross section continuity equation (Sherwin et al. 2003a)

$$\frac{\partial A}{\partial t} + \frac{\partial}{\partial x}\left(\overline{V}A\right) = 0; \qquad A = A_0(1+\eta)^2 \tag{5}$$

where η is the circumferential strain (normal wall displacement normalized to radius R), A, A_0 cross-sectional areas in the loaded and the stress-free conditions. Constitutive "tube model", closing these two equations for unknown variables A, P and $\overline{V}$, follows from the analysis of a solid domain.

2.2.2 Solid domain: the hyperelastic Fung's model and the generalized tube law

Consider a circular thin-wall cylinder in the polar system of coordinates. Let R be the radius of the wall under the load, R_0 – radius in a load free state, h - the wall thickness, ρ_w-density of the wall. Introducing wall kinetic energy K, elastic energy U_{el}, dissipative energy U_d and work of external load W_p, the Lagrangian density function relating to the solid domain can be presented as

$$L_s = \delta K - \left(\delta U_{el} + \delta U_d - \delta W_p\right) \tag{6}$$

The normal velocity of the moving wall $R_0 \frac{d\eta}{dt}$ defines kinetic energy per unit length

$$K = \frac{1}{2}\rho_w h {R_0}^2 \left(\frac{\partial \eta}{\partial t}\right)^2 \tag{7}$$

Internal elastic energy is composed of a hyperelastic strain energy (Fung et al. 1979) and energy, accumulated by a longitudinal prestress force N per unit area

$$U_{el} = \frac{hc}{2}\left(e^Q - 1\right) + N\left(\sqrt{1 + {R_0}^2\left(\frac{\partial \eta}{\partial x}\right)^2} - 1\right) \tag{8}$$

Here, $Q = a_{11}\epsilon_\theta^2 + 2a_{12}\epsilon_\theta\epsilon_x + a_{22}\epsilon_x^2$, and $c,\ a_{11},\ a_{12},\ a_{22}$ are material constants from Fung's anisotropic model (Fung et al. 1979), where ϵ_θ and ϵ_x are the circumferential and axial strain components. Strain energy of the wall modeling as a system of independent hyperelastic rings is simplified in a 1D case by setting $a_{12} = a_{22} = 0,\ \epsilon_\theta = \eta$, where η is the circumferential strain. As a result, for small strains ${R_0}^2\left(\frac{\partial \eta}{\partial x}\right)^2 \ll 1$, arriving at the expression for the strain energy of a reduced model

$$U_{el} = \frac{hc}{2}\left(e^{a_{11}\eta^2} - 1\right) + N\frac{{R_0}^2}{2}\left(\frac{\partial \eta}{\partial x}\right)^2 \tag{9}$$

Elementary work produced by the viscous component of circumferential stress relating to the Voight-type viscoelastic material and an external pressure reads

$$\delta U_d\text{-}\delta W_p = \left(\frac{h}{R_0}\Gamma\frac{\partial \eta}{\partial t} - P\right)R_0\delta\eta \tag{10}$$

where Γ is the viscosity constant. Calculating variational derivative of the Lagrange function L_s (Eq. (6)) ($L_s = L_s(\eta, \eta_t, \eta_x), \eta_t = \frac{\partial \eta}{\partial t}, \eta_x = \frac{\partial \eta}{\partial x}$)

$$\frac{\delta L_s}{\delta \eta} = \frac{\partial L_s}{\partial \eta} - \frac{\partial}{\partial t}\frac{\partial L_s}{\partial \eta_t} - \frac{\partial}{\partial x}\frac{\partial L_s}{\partial \eta_x} = 0 \tag{11}$$

obtains the of motion of an axisymmetric cylinder

$$P = \frac{h}{R_0}\left(ca_{11}\eta e^{a_{11}\eta^2} + \Gamma\frac{\partial \eta}{\partial t}\right) + \rho_w h R_0 \frac{\partial^2 \eta}{\partial t^2} - N{R_0}^2\frac{\partial^2 \eta}{\partial x^2} \tag{12}$$

The physics-based "tube law" follows now from Eq. (12), where we ignore expansion terms of the fifth degree in η and higher

$$P = \frac{h}{R_0}\left(ca_{11}\eta e^{a_{11}\eta^2} + \Gamma\frac{\partial \eta}{\partial t}\right) = \frac{h}{R_0}ca_{11}\eta\left(1 + a_{11}\eta^2\right) + \frac{h\Gamma}{R_0}\frac{\partial \eta}{\partial t} + O(\eta^5) \tag{13}$$

Note that partial derivative of the circumferential stress, $\sigma_\theta = \frac{PR_0}{h}$, by circumferential strain, η, at a zero load represents tangential modulus, $\overline{E}$, at a stress-free state (ν_P is the Poisson's ratio)

$$P\frac{\partial\left(\frac{PR_0}{h}\right)}{\partial \eta}|_{\eta\to 0} = ca_{11} = \overline{E}, \qquad \overline{E} = \frac{E}{1 - {\nu_P}^2} \tag{14}$$

According to Eqs. (13) and (14), the constitutive model is presented as a superposition of a viscoelastic and a

hyperelastic terms characterized by the Fung's hyperelastic coefficient a_{11} and a tangential modulus $\overline{E}$

$$P = \frac{h}{R_0}\overline{E}\eta e^{a_{11}\eta^2} = 2\rho_f c_{mk}^2 \eta e^{a_{11}\eta^2} + 2\rho c_{mk}^2 \frac{h\Gamma}{R_0}\frac{\partial \eta}{\partial t}$$
or in a truncated form (15)
$$P \cong 2\rho c_{mk}^2 \eta\left(1 + a_{11}\eta^2\right) + 2\rho_f c_{mk}^2 \beta \frac{\partial \eta}{\partial t} + O(\eta^5)$$

Here, $c_{MK} = \sqrt{\frac{\overline{E}h}{2\rho R_0}}$ – the Moens-Korteweg speed of pulse wave propagation, $\beta = \frac{\Gamma}{\overline{E}}$. By setting $a_{11} = 0$, replacing $\eta = \sqrt{\frac{A}{A_0}} - 1$, we retain the classic form of the *tube law* for linear viscoelastic material (Alastruey et al. 2011). Specifying in addition $\beta = 0$ results in a linear elastic tube law

$$P \cong 2\rho_f c_{mk}^2 \eta \tag{16}$$

2.2.3 Reorganizing the hyperelastic vessel formulation

In the following, we simplify the notation by denoting the cross-sectional area averaged axial velocity by V instead of $\overline{V}$. Assuming the generalized Hagen-Poiseuille radial velocity profile with $\gamma = 9$, justified by (Smith et al. 2002), and neglecting contribution of the axial stress component compare to the shear stress, Eqs. (4) and (5) read

$$\frac{\partial \boldsymbol{Q}}{\partial t} + \frac{\partial F(\boldsymbol{Q})}{\partial x} = \boldsymbol{f};$$
$$\boldsymbol{Q} = \begin{bmatrix} A \\ V \end{bmatrix};\ \boldsymbol{F} = \begin{bmatrix} AV \\ \frac{V^2}{2} + \frac{P}{\rho_f} \end{bmatrix};\ \boldsymbol{f} = \begin{bmatrix} 0 \\ -\frac{22kV}{A} + g_\tau \end{bmatrix}; \tag{17}$$

Here, $P_A = \frac{\partial P}{\partial A}$, and $A = A_0(\eta + 1)^2$. f relates to the viscous source term (Alastruey 2006), where $k = -22\pi\nu$ (since $\gamma = 9$), and kinematic viscosity $\nu = \frac{\mu}{\rho}$.

2.2.4 The characteristic analysis

When enforcing numerical algorithm to the hyperbolic system, it is useful to invoke the characteristic variables, while applying the characteristic properties to the time marching algorithm and implementation of boundary conditions. Considering arbitrary pressure – area relationship, $P = P(A)$, rewrite the homogeneous system of Eq. (17) in the following nonconservative quasi-linear form

$$\frac{\partial A}{\partial t} + V\frac{\partial A}{\partial x} + A\frac{\partial V}{\partial x} = 0$$
$$\frac{\partial V}{\partial t} + V\frac{\partial V}{\partial x} + \frac{P_A}{\rho_f}\frac{\partial A}{\partial x} = 0 \tag{18}$$

where $P_A = \frac{\partial P}{\partial A}$. Multiplying each equation in system of Eq. (18) by unknown coefficients $l_1$andl_2, respectively, create a linear combination

$$\left[l_1\frac{\partial A}{\partial t} + \left(l_1 V + l_2\frac{P_A}{\rho_f}\right)\frac{\partial A}{\partial x}\right] + \left[l_2\frac{\partial V}{\partial t} + (l_2 V + l_1 A)\frac{\partial V}{\partial x}\right] = 0 \tag{19}$$

Now associate each bracket of Eq. (19) with a substantial derivative of a relating variable

$$l_1\frac{dA}{dt} = l_1\frac{\partial A}{\partial t} + \left(l_1 V + l_2\frac{P_A}{\rho_f}\right)\frac{\partial A}{\partial x};$$
$$l_2\frac{dV}{dt} = l_2\frac{\partial V}{\partial t} + (l_2 V + l_1 A)\frac{\partial V}{\partial x} \tag{20}$$

The latter is equivalent to the eigenvalue problem, where the eigenvalue $\lambda = \frac{dx}{dt}$ determines direction of the wave propagation in a time -space domain (t, x)

$$l_1 V + l_2\frac{P_A}{\rho} = \lambda l_1$$
$$l_1 A + l_2 V = \lambda l_2 \tag{21}$$

By equating to zero, the relating determinant

$$\begin{Vmatrix} V - \lambda & \frac{P_A}{\rho_f} \\ A & V - \lambda \end{Vmatrix} = 0 \tag{22}$$

obtains two characteristic directions

$$\lambda_{1,2} = \left(\frac{dx}{dt}\right)_{1,2} = V \pm \sqrt{\frac{AP_A}{\rho_f}} \tag{23}$$

Once eigenvalues found, the normalized eigenvector components follow from Eq. (21)

$$l_1 = \pm\sqrt{\frac{P_A}{A\rho_f}}, \qquad l_2 = 1 \tag{24}$$

Compatibility conditions for nonlinear hyperbolic equations can be determined by integrating the differential form following from Eqs. (19), (20), (24)

$$l_1 dA + l_2 dV = \pm\sqrt{\frac{P_A}{\rho_f A}}dA + dV = 0 \tag{25}$$

So that the characteristic (Riemann) variables $W_{1,2}$ read

$$W_{1,2} = V \pm \int \sqrt{\frac{P_A}{\rho_f A}}dA \tag{26}$$

With an employment of the hyperelastic constitutive model (*i.e.,* no viscoelasticity), Eq. (15), consider pressure as a function of area, and its derivative in an expanded form of the exponential

$$P = 2\rho c_{mk}^2 \left[\left(\sqrt{\frac{A}{A_0}} - 1 \right) + a_{11} \left(\sqrt{\frac{A}{A_0}} - 1 \right)^3 \right]$$
$$P_A = \frac{\partial P}{\partial A} = \frac{\rho c_{mk}^2}{\sqrt{A} A_0} \left[1 + 3a_{11} \left(\sqrt{\frac{A}{A_0}} - 1 \right)^2 \right] \tag{27}$$

By substituting Eq. (27) into Eqs. (23) and (26), we obtain velocities of two simple waves propagating in opposite directions, and characteristic variables

$$\lambda_{1,2} = V \pm c_{mk} \sqrt[4]{\frac{A}{A_0}} k_\lambda,$$
$$k_\lambda = \sqrt{1 + 3a_{11} \left(\sqrt{\frac{A}{A_0}} - 1 \right)^2} \tag{28}$$

$$W_{1,2} = V \pm 4c_{mk} \sqrt[4]{\frac{A}{A_0}} k_w,$$
$$k_w \cong 1 + a_{11} \left(1.5 + 0.3 \frac{A}{A_0} - \sqrt{\frac{A}{A_0}} \right) \tag{29}$$

Equations (28) and (29) pinpoint results of a mathematical analysis of the wave propagation in compliant hyperelastic arteries, filled with a moving incompressible fluid. Here, W_1 and W_2 propagate information on velocity and pressure from proximal to distal and distal to proximal locations, respectively. By setting hyperelastic material coefficient to zero, $\left(a_{11} = 0 \text{ or } k_\lambda = k_w = 1\right)$, the known expressions relating to the linear elastic arterial wall are obtained (Peiró and Veneziani 2009). Note that Eqs. (27) – (29) can also be presented in the exponential form of the hyperelastic constitutive model.

2.3 Numerical discretization: finite volume method

CardioFAN utilizes two numerical schemes to solve set of Eq. (17), for different purposes of arterial simulations. First method is a classical explicit Lax–Wendroff scheme, that is stable when reproducing a smooth transient solution and is a counterpart of the Taylor-Galerkin method. However, when resolving discontinuity in geometry, physical properties or the time-dependent load function Lax–Wendroff results in false spurious oscillations, giving physically unrealistic or unstable results (as shown in Sect. 3.1). In these cases, a monotonicity preserving total variation diminishing (TVD) modification of Lax–Wendroff scheme (Harten 1983; Roe 1984) is utilized to reduce the numerical dispersion. The latter is exceptionally important when modeling waves propagating through compliant sites that underwent endovascular aneurysm repair by arterial stent placement (Back et al. 1994). To expedite convergence to the pulsatile conditions, the linear acoustic solution (Mungkasi and Ningrum 2016) was used to initialize the time marching process based on the TVD Lax–Wendroff scheme. Discretization of the nonlinear set of Eq. (17) is discussed with more detail in appendix A. The comparison between the results obtained by TVD and classic Lax–Wendroff methods, in discontinuous waves, is detailed in our previous work (Liberson et al. 2017). In Sect. 3.1, the advantages of using TVD method against other non-TVD methods are explored for a manufactured case of a stented artery.

2.4 Boundary conditions

2.4.1 Inlet

Inlet flow rate is prescribed by enforcing known blood flow waveform,$Q(t)$, as a function of time at the inlet. At the root of aorta, this known variable is imposed at the edge of the first element. To calculate the inlet velocity and a cross section area, the flow rate equation is complemented by the backward running characteristic, as shown by Eq. (30). This assignment is previously shown to provide physiological waveform shapes (see (Willemet et al. 2011)).

$$V_{in} A_{in} = Q_0(t)$$
$$V_{in} - 4 \left[c_{MK} \left(\frac{A}{A_0} \right)^{\frac{1}{4}} \right]_{in} = \left(W_2 \right)_1 \tag{30}$$

where W_2 is the backward propagating invariant, Eq. (29), calculated at the first cell $n = 1$. In case of the hyperelastic form of the FSI formulation, Eqs. (28) and (29) are utilized, where Eq. (30) takes the following form

$$V_{in} A_{in} = Q_0(t)$$
$$W_2 = V - 4c_{mk} \sqrt[4]{\frac{A}{A_0}} k_w,$$
$$k_w \cong 1 + a_{11} \left(1.5 + 0.3 \frac{A}{A_0} - \sqrt{\frac{A}{A_0}} \right) \tag{31}$$

2.4.2 Outlet boundary condition (RCR lumped parameter model)

Three-element Windkessel model, characterized by resistance (R1), capacitance (CT) and second resistance (R2) (*i.e.,* RCR), is used to define the terminal BC at the truncated outlets. Details of different types of lumped parameter (*i.e.,* 0-Dimensional) terminal models can be found in (Grinberg and Karniadakis 2008; Alastruey et al. 2008). Eq. (32) presents the differential form of the boundary condition, comprising time-dependent pressure (P_e) and flow (VA) at the exit of the truncated vessel. The terminal condition is complemented by the forward propagating invariant W_1 arriving at the truncated section from the center of last cell, $n = N$, of the vessel

$$(\dot{VA})_T = \left[\frac{\dot{P}_e}{R_c} + \frac{P_e - P_{out}}{R_c R_p C_T} - \left(1 + \frac{R_c}{R_p}\right)\frac{VA}{R_c C_T}\right]_T \tag{32}$$

Arterial conduit resistance (R_C) and peripheral resistance (R_P) of the arteries need to be specified. One method is based on measurements of the mean arterial pressure (P_m), outlet pressure relating to microcirculation site, (P_{out}) and the mean flow at the root of the arteries ($\overline{Q}_{in}$). Total arterial compliance (C_T) can then be found by measuring the time of diastolic decay (τ) of the pressure (Xiao et al. 2014)

$$\begin{aligned} R_T &= \frac{P_m - P_{out}}{\overline{Q}_{in}}, \quad P_m = P_0 + \frac{1}{3}(P_s - P_d) \\ R_C &= \frac{\rho C_{Mk,\ seg}}{A_d}, \quad R_T = R_C + R_P C_T = \frac{\tau}{R_T} \end{aligned} \tag{33}$$

The conduit and peripheral compliances are calculated by a summation of the compliances of all 1D segments (Xiao et al. 2014)

$$\begin{aligned} C_T &= C_p + C_C, \quad C_c = \sum_{i=1}^{N} C^j_{seg}, \quad C^i_{seg} = \frac{A_d L}{\rho_f (C_d)^2}, \\ \tilde{C}^j &= C_P \frac{R_P}{R_C + R_P} = C_P \frac{\overline{Q}^j_{out}}{\overline{Q}_{in}} \\ A_d &= \frac{1}{L}\int_0^L A_d(x)dx, \qquad C_d = \frac{1}{L}\int_0^L C_d(x)dxe \end{aligned} \tag{34}$$

Here, A_d, C_d are the diastolic area and speed of wave propagation, $\overline{Q}^j_{out}$- the j^{th} segment outlet flow rate, and $\tilde{C}^j$ is the terminal compliance at the j^{th} segment

If measurement is not plausible, R_T and C_T can be approximated with the iterative method introduced by (Xiao et al. 2014). Terminal compliance is then corrected as follows

$$C^j = \tilde{C}^j \frac{R_P + R_C}{R_P} \tag{35}$$

Since Eq. (32) is a time-dependent differential equation, its discretized version is used at each time step. Being complemented by the forward propagating characteristic variables at the last cell, Eq. (32) can be solved for velocity and pressure, and thus cross-sectional area, at each time step. For simplicity, linear forward propagating characteristic (LeVeque 2002) can also be considered at the last cell.

2.4.3 Bifurcated joints

Splitting flow junctions are typical alignments in the arterial system. Let V_1, P_1 A_1indicate velocity, pressure and cross-sectional area of a parent vessel at the junction interface, andV_2, P_2 A_2, V_3, P_3 A_3 – the corresponding properties of daughter vessels at the interface. The following assumptions are made to simplify the junction matching procedure: 1) energy losses at the junctions are ignored (Matthys et al. 2007), 2) pressure changes across the junction is neglected, $P_1 = P_2 = P_3 = P$. Since the pressure values algebraically relate to the cross-sectional areas, (Eq. (15)), there are only four independent quantities V_1, V_2, V_3, P which need to be specified. To close the problem, the conservation of mass and extrapolation of forward and backward propagating invariants present,

$$\begin{aligned} &V_1 A_1 = V_2 A_2 + V_3 A_3 \\ &V_1 + 4\left[c_{MK_1}\left(\frac{A}{A_0}\right)^{\frac{1}{4}}\right]_1 = W_1, \\ &V_{2,3} - 4\left[c_{MK_{2,3}}\left(\frac{A}{A_0}\right)^{\frac{1}{4}}\right]_2 = \left(W_2\right)_{2,3} \end{aligned} \tag{36}$$

where $W_1$is the forward running invariant calculated at the center of the last cell of a parent vessel (vessel 1); $\left(W_2\right)_{2,3}$ are the backward running invariant calculated at the first cell of the daughter vessels (vessels 2 and 3)

2.4.4 Connectivity matrix and specification of the segment properties

The connectivity condition of the small segments is vital for generating a patient-specific network of vessels to solve the set of governing equations. The following properties are assigned for each vessel inside matrices, to account for the variations over the elements of each segment. The properties of interest for each segment are its length, speed of pulse

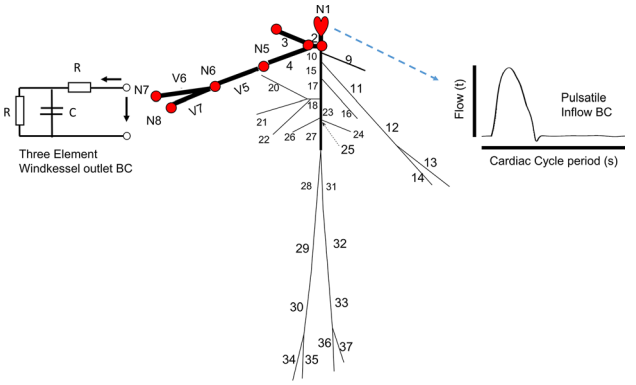

Fig. 1 Example of the 37 main arteries geometry generated by connecting nodes and vessels in one matrix. Each node will fill out the information required for 1 row of the following matrix: [Node# Upstream-Vessel# First-Downstream-Vessel# Second-Downstream-Vessel#] Inflow flow boundary condition (BC) is imposed at the first node, and three-element Windkessel model at truncated locations

wave propagation in that vessel and angle from the reference point. In addition, cross-sectional area (as a function of the axial distance) of the segments from their initial point, connectivity matrix describing the connection of nodes to vessels and to each other (shown in Fig. 1) and terminal resistance and compliances are defined as inputs to the model.

3 Results and discussion

Peripheral pressure measurements, with techniques such as upper arm or wrist cuff BP monitors, can provide estimates of the central systolic and diastolic pressure, while applanation tonometry can obtain the pressure pulse waveform. This information is usually used for calibrating (Funamoto and Hayase 2012) a computational model or for data assimilation purposes (Vennin et al. 2015). Although usually used by clinicians, pulse-wave amplification at the peripheral artery renders peripheral measurements inadequate to represent the aortic or central arterial pressures (Sharman et al. 2008; McEniery et al. 2008). In addition, antihypertensive medications have different effects on central pressure despite similar reductions in brachial blood pressure (Reule and Drawz 2012). Central aortic pressure is a better predictor of cardiovascular outcome after any alterations in the normal/resting functionality of the cardiovascular system (Sharman et al. 2008; Nelson et al. 2010). Thereby, this is essential to develop a reliable noninvasive method to measure the central blood pressure contrary to the currently available invasive catheter method (McEniery et al. 2014). The first step is to develop a computational hemodynamics-based approach for *data assimilation*, requiring a reliable computational framework. To evaluate the accuracy of the computational model, the patient-specific calibration and computational results validation against a manufactured case of stented artery and three well-known cases of arterial networks in the literature are presented here:

1. **Manufactured case of stented artery** We demonstrate the blood flow and pressure waveforms in reduced-order arterial system models with stents, as an example of arteries with discontinuous vessel wall properties. We validate and compare the results of the TVD Lax–Wendroff-based solver against a manufactured exact solution, and other non-TVD numerical schemes such as Lax–Wendroff and MacCromack (Sect. 3.1).
2. **Numerical** The blood flow and pressure in 55 main arteries of a human body are simulated (Sect. 3.2). The results are compared against the numerical work, provided by a discontinuous Galerkin model presented by (Alastruey et al. 2012) and (Sherwin et al. 2003b).
3. ***In vitro*** Blood flow and pressure in 37 main arteries of the human body are simulated, calibrated and compared against an *in vitro* model of the 37 arteries, developed by Matthys et al. (Matthys et al. 2007) (Sect. 3.3).
4. ***In vivo*** A patient-specific model is generated, using MRI-based measurements of the arterial diameters and flow along the aorta and pressure measurements at supra-aortic vessels, as presented in (Alastruey et al. 2016). The blood flow model results are compared against the measurements and show improvements compared to prior numerical predictions (Sect. 3.4).

As demonstrated here, reduced-order blood flow simulation platform, CardioFAN, provides accurate prediction of blood flow and pressure. This includes the range, systolic and diastolic values and the shape of the waveforms in all three cases and the luminal area values for *in vivo* case, where clinical measurements are available to compare.

Computational Framework Specifications: Mesh-dependence was studied to achieve reliable results for each of the large arterial networks. The Lax–Wendroff version of the code performs calculations for all vessels during five cardiac cycles in less than 5 minutes and with a normal 4 CPU cores, 16 GB RAM personal computer (PC). Numerical PTT calculations and viscoelastic calculations can be set to on or off, which affect the computation time. CardioFAN is accessible through the provided links[1].

3.1 Discontinuous arterial wall properties

Time marching methods are applied to model pulsatile hemodynamic flow in a stented elastic artery. The

[1] CodeOcean Repository: CodeOcean
Github (Zenodo) Repository: Zenodo

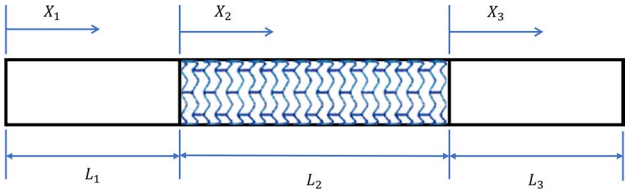

Fig. 2 Schematics and dimensions of a hypothetical stented artery

Moens-Korteweg speed of propagation exhibits jumps due to the difference in compliance between "rigid" stent and a "soft" arterial wall. It is also possible to abruptly change the speed of propagation due to the change of the cross-sectional area in case of certain pathologies, e.g., stenosis or an aneurism. Compliance discontinuity is currently being handled in two ways in the literature: 1) data regularization, where the properties across the junction interface are artificially smoothed to eliminate discontinuity (Tortoriello and Pedrizzetti 2004), 2) domain decomposition, where the coupling between two segments is accomplished providing flow and momentum continuity across the interface (Formaggia et al. 2003). However, the algorithm utilized here is a regular time marching method applied to the system of partial differential equations with variable coefficients and without any preliminary regularization or domain splitting.

We consider a tube model consisting of 3 segments, as shown in Fig. 2. The middle segment represents a vascular stent implanted into the arterial vessel. After a few months of the stent implantation, the stent struts fuse with the tissue growth creating a composite structure with relatively rigid monolithic properties within an elastic arterial tube. Each segment relates to the local spatial coordinate x_i, $0 \le x_i \le L_i$, $i = 1, 2, 3$ as shown in Fig. 2. The Moens-Korteweg velocity of propagation at each segment is denoted by $c_{MK,i}$.

For numerical results, we take $L_1 = L_3 = 0.2\,m$, $L_2 = 0.05\,m$; $c_{MK,1} = c_{MK,3} = 4\frac{m}{s}$, $c_{MK,2} = 10m/s$; $\rho = 1000\frac{kg}{m^3}$; $A_0 = 0.0314\,m^2$. The total number of uniformly distributed computational cells is set to $N = 90$. Inlet boundary condition for the volume rate and exit boundary condition for the pressure are given in Appendix B by equations (B7) and (B8), where $Q_0 = 50\frac{mL}{s}$, $\overline{p} = 13.3\,kPa$, $p_a = 2.66\,kPa$ are the flow rate, mean aortic blood pressure and magnitude of the pulse pressure, respectively. The Courant-Friedrichs-Lewy number calculated based on the wave speed of propagation inside stent is $CFL = 1$.

Figure 3 presents solution of the linearized problem for the pulsatile flow inside stented artery, obtained by three different numerical methods. Second-order approximation schemes such as Lax–Wendroff and MacCormack, giving an accurate result for the smooth solutions (LeVeque 2002), fail near discontinuities where spontaneous oscillations are generated. The TVD scheme apparently has an advantage keeping the solution varying monotonically as seen in Fig. 3c.

In the second test, we imposed the same arterial wall properties as in linear case, for a model of stented artery with the nonlinear governing equations to describe its FSI

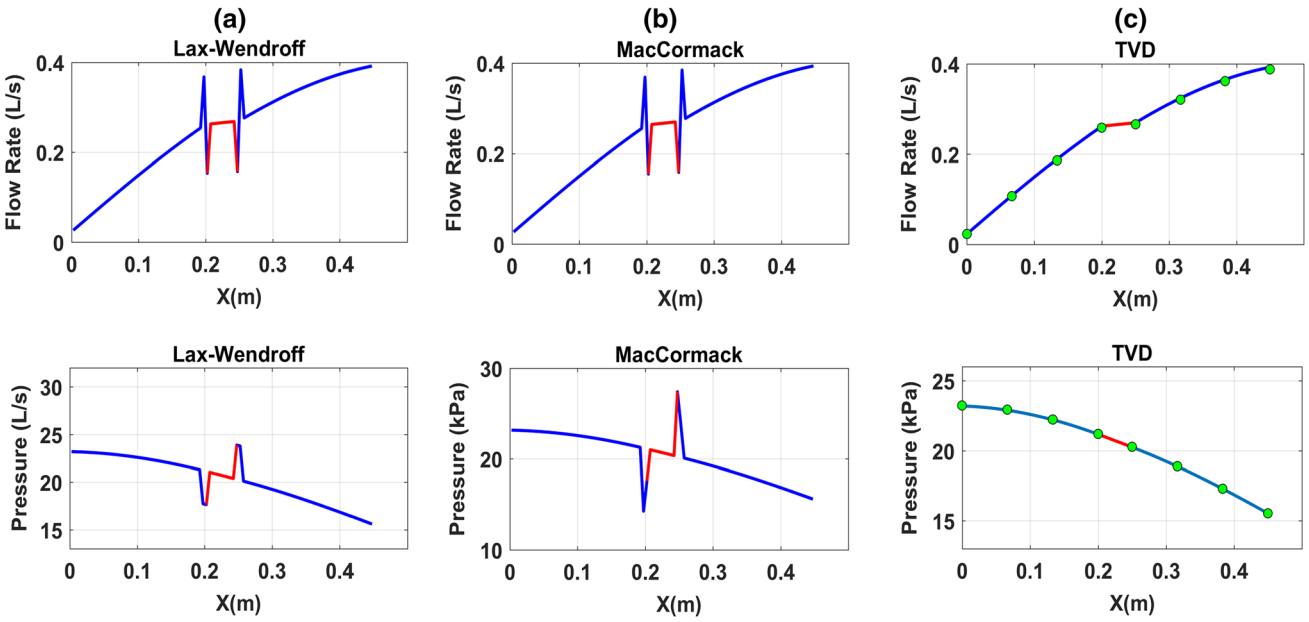

Fig. 3 Test on numerical resolution with different methods in case of a stented artery. **a** Lax–Wendroff, **b** MacCormack, **c** TVD method (circles) vs closed-form solution (solid line). Results are shown at physical time t=1 s

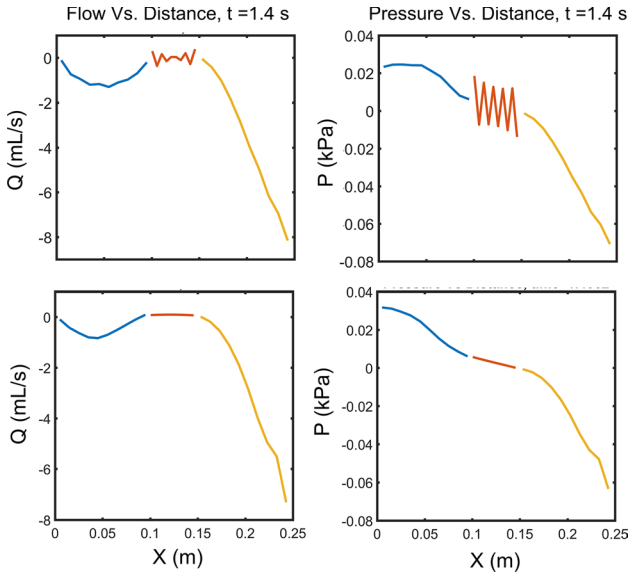

Fig. 4 Test on numerical resolution in case of the nonlinear model of a stented artery. (top) Lax–Wendroff, (bottom) TVD Lax–Wendroff with van leer flux limiters. Pressure and flow results are shown at physical time t=1.4 s. Blue and yellow lines indicate normal artery wall and the middle orange line indicates the stented portion of the artery

behavior. A half-sine flow wave with a maximum magnitude of 250 mL/s was imposed at the inlet, accompanied by a non-reflective outlet BC. Flow and pressure results were recorded along the tube axis in different instances of time. Figure 4 illustrates a comparison between the results of a second-order Lax–Wendroff and a nonlinear TVD Lax–Wendroff (Eqs. (A5)–(A7) in "Appendix A"). The artificial oscillations in the Lax–Wendroff compared to nonlinear TVD method shows the sensitivity of non-TVD methods to discontinuity in properties, suggesting the benefit of using TVD schemes for arterial models with discontinuous wall properties.

3.2 Validation against numerical data of 55 main human arteries

The model for 55 main arteries is presented by (Sherwin et al. 2003b), (Reymond et al. 2009) and (Alastruey et al. 2012) based on physiological input data extracted from a young healthy patient. They also show a numerical model of the network which was validated with available MRI data for flow and pressure data at the peripheral locations (Reymond et al. 2009). Here, this model is recreated in CardioFAN by defining the connectivity matrix and input parameters based on the network presented in (Alastruey et al. 2012).

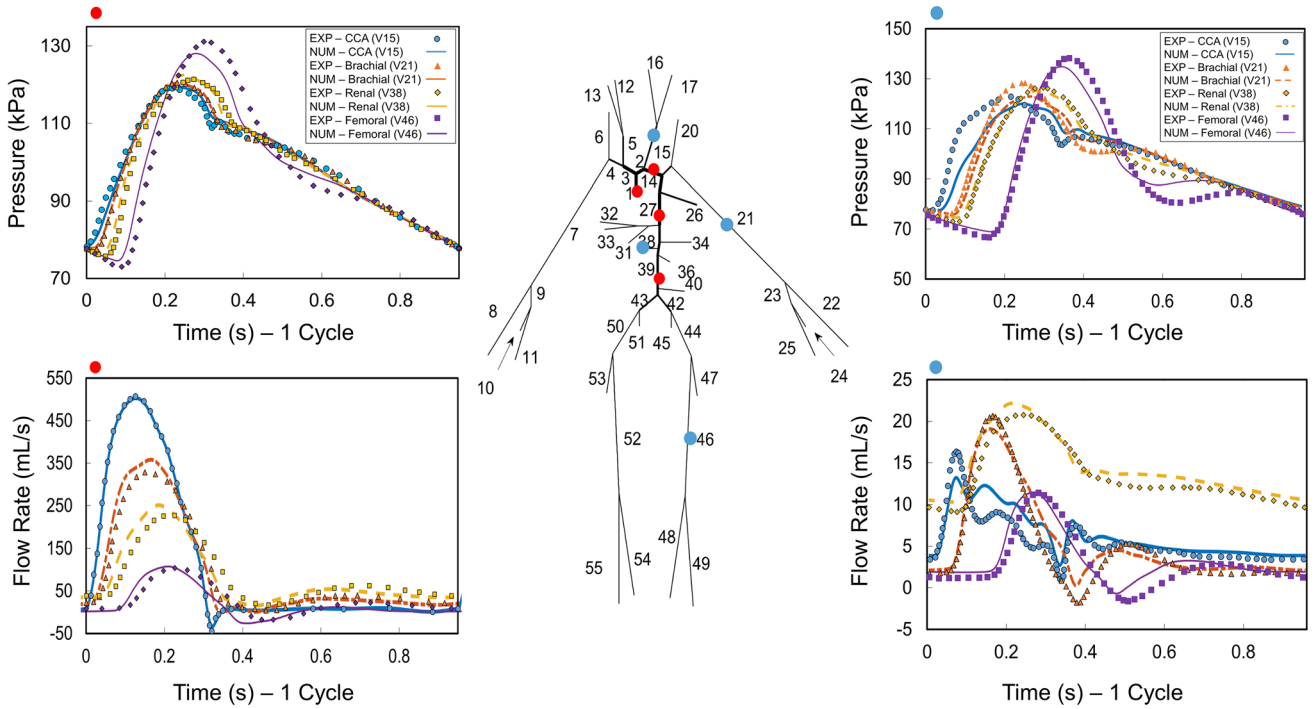

Fig. 5 Schematics and validation of the 55 segments model of human arteries. The model is recreated based on the arterial network presented in (Alastruey et al. 2012). Evaluated points along the aorta are indicated with red circles and presented at the left side (P at top and Q at bottom). Carotid aorta, left brachial artery, renal and femoral arteries, vessels 15,21,38,46, highlighted by blue dots and presented at the right side. Dotted markers represent the original data, and solid lines are the results obtained using CardioFAN (view the colored plots in online version)

Vessel properties, such as vessel lengths, radii and speed of propagation at each segment, are provided as inputs to the software (check the link to CardioFAN for testing the code for 55 vessels). At the ascending aorta, the flow as a function of time is imposed for one cardiac cycle and at the terminal boundaries, resistances and compliances for the RCR model are specified. Figure 5 demonstrates results provided by CardioFAN overlaid on top of the numerical results previously presented by (Alastruey et al. 2012).

As shown in Fig. 5, a good agreement between the results from CardioFAN and the numerical results from (Alastruey et al. 2012) was obtained. These results clearly capture features such as systolic peak an diastolic decay and the dicrotic notch, better than our previously presented Lax–Wendroff-based linear elastic numerical simulation (Vahedein and Liberson 2018a). In contrast to the recreated work, instead of viscoelastic properties, we were able to retrieve the systolic peak for the data in peak of the pressure waveform (*e.g.,* femoral artery, purple plot in top right), by correct selection of Fung parameter "*a*" (selected to be in 1.3-1.8 range, extracted from (Dúóng et al. 2017)). Although CardioFAN is capable of solving viscoelastic arterial wall properties, it has minor effect on the flow and pressure in large arteries (Bergel 1961), or in higher frequency waves (Ghigo et al. 2016). Therefore, neglecting the viscoelastic properties, we were able to reduce the computational time significantly while getting accurate predictions compared to a model with viscoelastic properties.

3.3 Validation against in vitro data of 37 main human arteries

We compare a numerically recreated model of 37 main arteries, with an experimental silicone-based compliant model of the arteries (Matthys et al. 2007). Water-glycol mixture with a density of $\rho = 1050$ kg m $^{-3}$, and viscosity of $\mu = 2.5$ mPa s was used to imitate blood (for more details on experimental setup, refer to (Matthys et al. 2007)). Simple terminal resistance tubes provisioned for this model allows the experimental model of Matthys et al., to reproduce the main features of pressure and flow, as observed *in vivo* (such as the dicrotic notch, diastolic decay and peaking and steepening of pulse pressure away from the heart). Here, the properties of these vessels, such as, vessel length, radii, and wall thickness (see (Matthys et al. 2007) or (Alastruey et al. 2011)), are used to recreate this network of arteries. At the inlet, we have prescribed a given flow waveform, resulting in 70 beats per minute with stroke volume of 70 ml at the root. Similar to experimental setup, simple resistance terminal boundary conditions are imposed to numerical model. The simple resistance tubes at the experimental setup produce non-physiological oscillations at the peripheral locations (as mentioned by Matthys et al.); however, our code is able to capture the frequency of these oscillations. Energy losses at the network bifurcations have secondary effect on flow and pressure waveform predictions (as shown by Matthys et al.) and therefore not considered here. Resulting waveforms are presented in Fig. 6, at different locations along the arterial tree.

Good agreement is obtained between numerical predictions and the experimental data for blood pressure and flow rate in various parts of the 37 arteries model. We see that the numerical model can completely capture the pressure waveform features, such as systolic peak, dicrotic notch and the diastolic decay of the waveforms. On the other hand, flow oscillations are fully captured, with magnitude being overpredicted at the most peripheral locations. The flow waveform errors are in complete agreement with numerical model developed by (Matthys et al. 2007; Alastruey et al. 2011) for the same *in vitro* data, and as mentioned before, relates to the discrepancies in flow waveform measurements. The averaged relative root mean squared errors over all segments in each network generation sequence, calculated at the experimental measurement locations was previously reported as not exceeding 4% for pressure and 19% for flow predictions. The individual errors for each segment was reported in (Alastruey et al. 2011), showing a range of 4.7 to 35.3% error in flow rate predictions. For CardioFAN, averaged relative RMSE in the evaluated locations are provided in Table 1. The errors are smaller than the previously reported values, even in the location of abdominal aorta and without using a viscoelastic model, except for Left Ulnar artery location.

Compared to pressures, the larger errors demonstrated in flow rate predictions correlate with the large uncertainties in experimental measurement of flow waveform (Matthys et al. 2007). The standard deviation of these measurements, captured with an ultrasonic volume flow meter, have not been displayed here (they can be viewed in (Matthys et al. 2007)). In addition, viscoelastic solver may help in improving the results of oscillating flow locations, especially since the experimental setup was designed with viscoelastic material (Alastruey et al. 2011).

3.4 Validation against in vivo data of 26 main human arteries

The 26 segments model, comprising aorta and supra-aortic segments, has been created based on the *in vivo* data presented by (Alastruey et al. 2016). To minimize uncertainty in their *in vivo* acquisition of noninvasive hemodynamic data, a rich array of 3D and 2D SSFP MRI

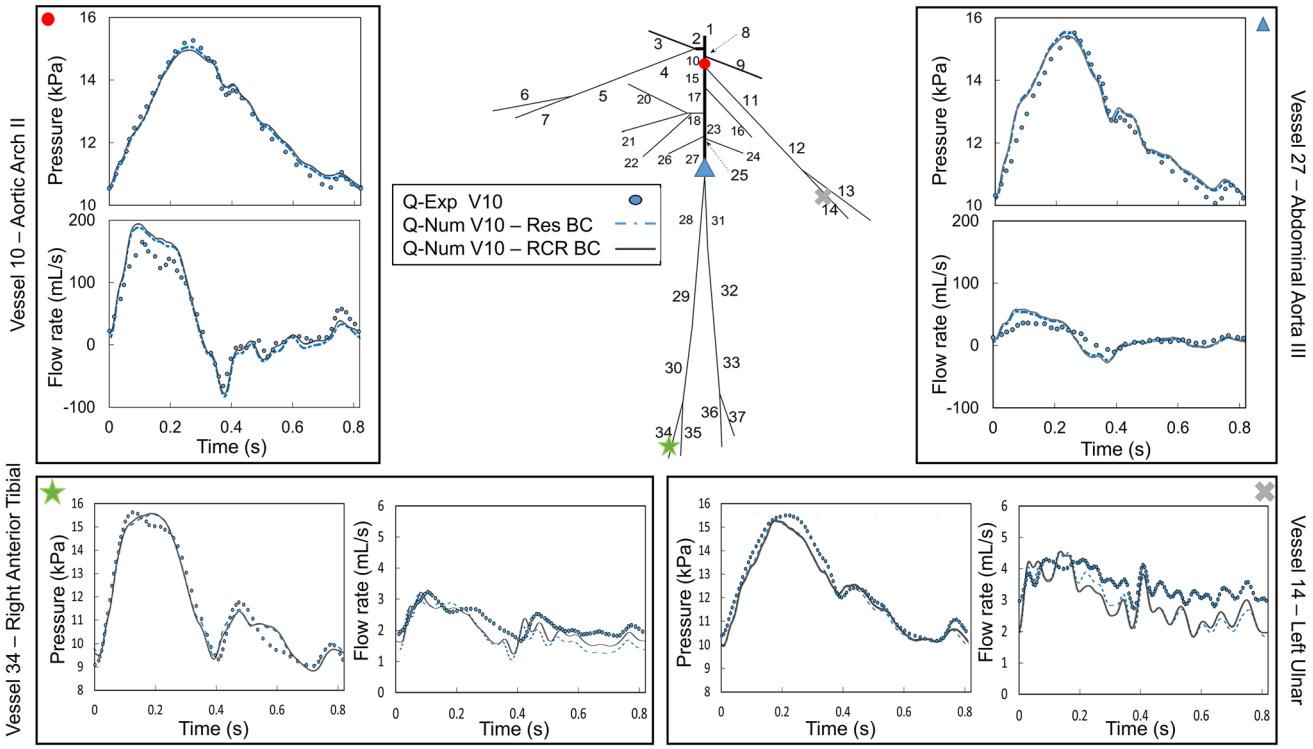

Fig. 6 Schematics and validation of the 37 segments model of human arteries. Model recreated based on the in vitro network presented in (Matthys et al. 2007). Evaluated points along are marked by red circles. P and Q plots are shown for vessels 10-14-27-34, representing aortic arch II, left ulnar artery, abdominal aorta III and right anterior tibial arteries. Blue markers represent the original *in vitro* data, whereas, solid lines and dotted lines represent the results obtained using CardioFAN with RCR and R terminal boundary models, respectively (view the colored plots in online version)

Table 1 Average relative errors of the numerical pressures and flows in all the evaluated locations of the network

Location	$\bar{\epsilon}$ *pressure* (%)		$\bar{\epsilon}$ *flow* (%)	
Aortic Arch II	**0.89**	1.15	**9.40**	8.83
Abdominal Aorta III	**1.49**	1.75	**20.46**	24.20
Left Ulnar	**2.24**	2.47	**12.02**	12.73
Right anterior tibial	**1.53**	1.82	**10.10**	7.41

Average relative errors in flows are calculated with respect to experimental data and local maximum as proposed in (Xiao et al. 2014). Bold numbers refer to the Resistance (R) terminal boundary model and normal text relate to RCR terminal boundary model, with a constant compliance C=10^{-11} m^3 Pa^{-1}

clinical data was used to create the subject-specific geometry. Heart rates have been measured by MRI and applanation tonometry and the flow rate measured using PC MRI. This resulted in a more consistent determination of cross-sectional area distributions and flow rates across the aorta, which serves as the input for numerical modeling and computational results validation.

3.4.1 Preparing the input parameters and boundary conditions

In order to extract model input parameters, the method presented by (Xiao et al. 2014) is used for calculating individual resistances and compliances at the truncated arteries (as explained in Sect. 2.4.2). In (Alastruey et al. 2016), the speed of wave propagation at each segment was prescribed based on a foot-to-foot method (Gaddum et al. 2013) as a constant value. Here, we suggest an improved method for calculating the speed of propagation in section 3.3.2, which results in a better prediction of the flow rate, cross-sectional area and pressure waveforms along the flow path. Recreated model using CardioFAN is able to test the accuracy of the code against the actual patient-specific data. The properties of each segment were assigned based on the data presented in (Alastruey et al. 2016). Following Alastruey et al., we have adopted two of the most successful simulation cases:

1. *BEST AREA* Outlet pressure is selected to be equal to capillary pressure commonly used at the outlet of 1D models (Parazynski et al. 1993), P_{out} = 4400 kPa. The total resistance and compliance parameters are altered iteratively (according to the technique introduced by

(Xiao et al. 2014)), to match the diastolic pressure and the range of pressure at the carotid artery location, where the *in vivo* data was available. To comply with the recreated work this method is named *BEST AREA*, since it provides the most accurate cross – sectional area and flow predictions.

2. *BEST PRESSURE* Outlet pressure is selected to be equal to the average value of the fitted pressure to the diastolic decay of the supra-aortic pressures as a function of time, captured using applanation tonometry. This pressure is $P_{out} = 9200$ kPa, and the total resistance and compliance parameters are not required to be altered (or need a few iterations) since the outlet pressure is a patient-specific value.

   This prescription of the boundary conditions is named as *BEST PRESSURE*, since it provides the most accurate prediction of the pressure waveform at the left carotid artery.

P_{out} (outlet pressure at exit branches),$\overline{Q}_{out}$ (mean outlet flow rate at exit branches) and $\overline{Q}_{in}$, (the mean flow rate at the aortic root) are all measured by (Alastruey et al. 2016). This enables the calculation of peripheral resistance and compliances for each outlet segment (see Sect. 2.4.2). The algorithm for calculating the RCR parameters is embedded in CardioFAN.

3.4.2 Improved method for calculating the speed of propagation

Foot-to-foot method was previously used by (Alastruey et al. 2016) to assign the Moens-Korteweq speed of propagation (C_{mk}) as the speed of sound in a fluid–structure interaction system. The evaluated flow waveforms for foot-to-foot method were related to the path connecting the ascending aorta to the abdominal aorta (Asc 1 to Desc 4 in Fig. 5).

Numerically calculated PWV have been previously used to validate experimentally measured PWV based on flow or pressure waveforms (Trachet et al. 2010; Obeid et al. 2017). It was illustrated in (Liberson et al. 2017) and (Lillie et al. 2016), that the modified value of the PWV calculated as the speed of a forward propagating Riemann invariant, can significantly improve prediction of the blood pressure as a function of the PWV.

Associating the measured speed of propagation values reported by (Alastruey et al. 2016) (named there as c_d) with the calculated PWV, Eq. (28) was used to recalculate the Moens-Korteweq speed of sound at each segment

$$\mathrm{PWV} = c_d = V + c_{mk}\sqrt[4]{\frac{A}{A_0}}k_\lambda \tag{37}$$

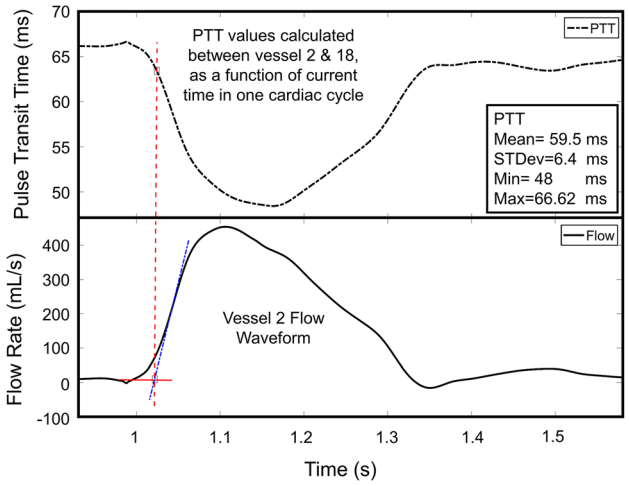

Fig. 7 PTT as a function of the calculation start time. The time during the second cardiac cycle is shown in the x-axis (top figure). The flow waveform corresponding to the same time scale is presented (bottom figure). The crossing of the maximum derivative of the flow waveform systolic rise and the extended horizontal line from diastolic flow is the start time of PTT calculation from foot-to-foot method, as shown by Alastruey et al. PTT calculation pathway is from ascending aorta (Asc Aorta 1) to the abdominal aorta (Desc Aorta 4)

Since the slope of a forward running characteristic line is determined by PWV

$$\frac{dt}{dx} = PWV^{-1}(x,t) \tag{38}$$

Equation (38) serves to calculate the PTT required for the pulse wave to propagate between two specified sections along the flow pathway. Using the second order of accuracy Heun's method (Chapra and Canale 1997), Eq. (38) is integrated by specifying the starting location for PTT evaluation.

Starting from $C_{MK} = c_d$, assigned in (Alastruey et al. 2016) for each segment, C_{MK} was incrementally reduced until the numerically calculated PTT matched the clinical value of 63 ms, obtained from foot-to-foot method (Gaddum et al. 2013). Foot-to-foot method includes deduction of the starting location for PTT evaluation. The numerically calculated PTT is shown in Fig. 7 as a function of the PTT calculation start time along the second cardiac cycle. The intersection of the maximum derivative of the flow waveform systolic rise and the extended horizontal line from diastolic flow is employed to pinpoint the PTT calculation starting point matching experimentally obtained foot-to-foot PTT.

Figure 7 shows that the computational PTT, based on the modified (reduced)C_{MK}, and relating to the same starting point as the experimental foot-to-foot method, matches the experimental value of$PTT \approx 63\ ms$.

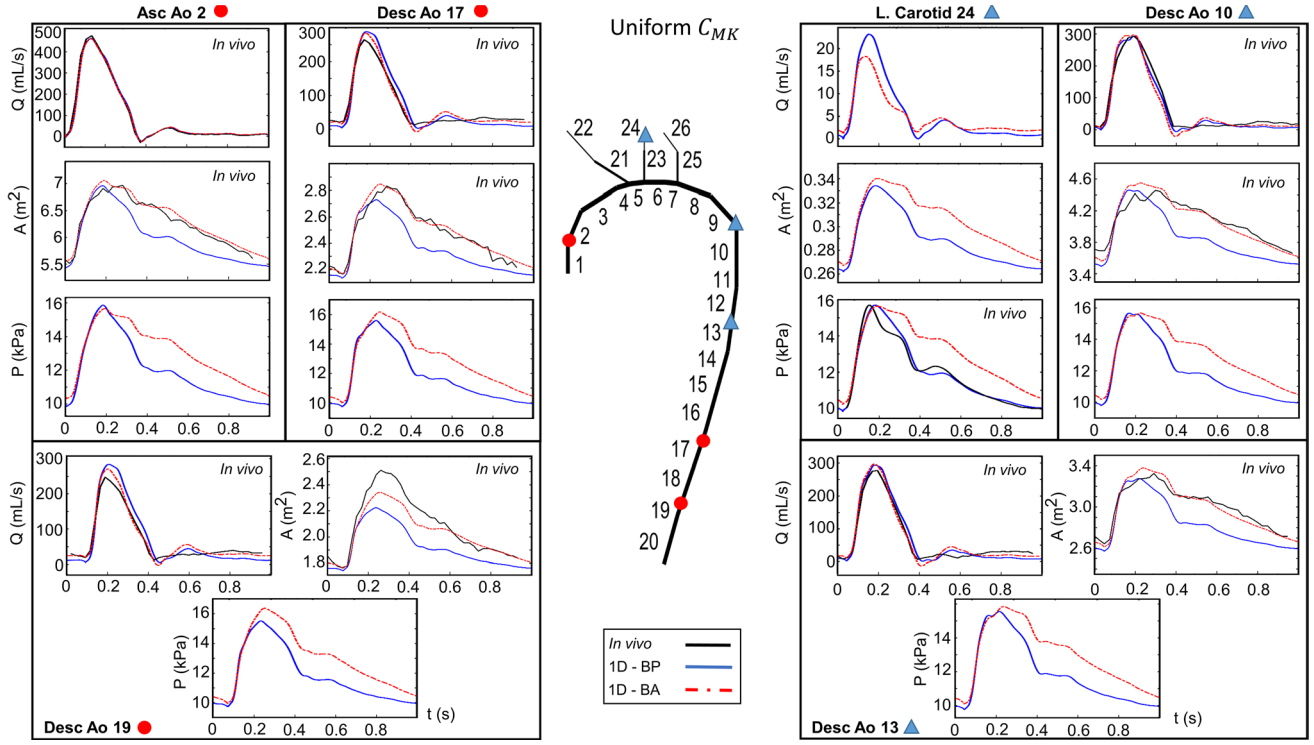

Fig. 8 Schematics and validation of the 26 segments model of arteries along the aorta and supra-aortic vessels with uniform speed of propagation. The model recreated in CardioFAN based on the same network presented in (Alastruey et al. 2016). Evaluated points on the left and right are specified on the schematics with red circles (segments 2-17-19) and blue triangles (segments 10-13-24), respectively. Pressure (P), flow (Q) and luminal area (A) plots show results of *BEST AREA* method (red dotted lines), *BEST PRESSURE* method (blue solid lines) and clinical *in vivo* measurements where available (black solid lines). Results are evaluated at the inlet of these segments, except for the common carotid artery, evaluated at the outlet of the segment (view the colored plots in online version)

Application of the described technique resulted in a 4.5% decrease in the speed of propagation, which corresponds to the 9.2% decrease in tangential modulus ($\overline{E}$), assigned at each segment. Therefore, instead of $C_{MK} = 4.56$ m/s, we use $C_{MK} = 4.36$ m/s in CardioFAN. Figures 5 and 6 show the resulted flow, cross-sectional area (luminal area) and pressures which imply improvement in predicting their waveform with corrected C_{MK}.

Another interesting result of this correction is for nonuniform values of c_d or PWV, previously presented by Alastruey et al. (2016). Although the individual values of the PWV for each segment were not measured, QA loop method Rabben et al. (2004) was used to provide C_d for all segments. We reduced the nonuniform C_{MK} (again starting from $C_{MK} = c_d$ values) with a single multiplier until the numerically calculated PTT matched the PTT from foot-to-foot method ($PTT = 63$ ms). As a result, the corresponding C_{mk} in all segments are found to be lower by 20% than the previously reported nonuniform C_d values. It also resulted in improved flow, luminal area and pressure predictions compared to the results presented in (Alastruey et al. 2016).

3.4.3 *in vivo* Validation results with BEST PRESSURE and BEST AREA cases

Uniform C_{MK} Figure 8 shows the results of both *BEST PRESSURE* and *BEST AREA* models for uniform speed of propagation (*i.e.,* arterial stiffness). The results relate to the corrected constantC_{MK} applied to all segments, with resistances and compliances calculated and matched at the terminal locations. The compliance and resistances are corrected with the iterative method described in (Xiao et al. 2014), to correctly capture waveform range and diastolic pressure, respectively. The corrected values are $R = 1 \times R_T$ and $C_j = C_j/1.5$ for *BEST PRESSURE* and $R = 3.3 \times R_T$ and $C_j = C_j/1.6$ for *BEST AREA* case. We have applied the Fung constant $a = 8$, and $a = 2$, respectively, to account for hyperelastic properties. These values are assigned as a constant number to all vessels. They were found iteratively by calibrating CardioFAN to the *in vivo* pressure data of the left carotid artery (*i.e.* segment #24). It should be noted that by having more PTT data available, the individual values of Fung hyperelastic constant can further improve the results.

The *BEST PRESSURE*, which prescribes a patient-specific terminal pressure measured at the common carotid

Table 2 Average relative errors of the numerical pressures, flows and luminal areas evaluated against clinical measurements along aorta and left common carotid artery

Location	$\bar{\varepsilon}$ *pressure* (%)		$\bar{\varepsilon}$ *flow* (%)		$\bar{\varepsilon}$ *area* (%)	
Asc Aorta (V2)	–	–	**1.13**	1.44	**1.00**	3.46
Desc Aorta (V10)	–	–	**5.13**	4.31	**1.61**	5.75
Desc Aorta (V13)	–	–	**3.72**	3.94	**1.38**	5.57
Desc Aorta (V17)	–	–	**3.49**	6.69	**1.10**	4.83
Desc Aorta (V19)	–	–	**4.11**	7.55	**2.73**	7.03
Left CCA (V24)	**8.79**	1.56	-	-	-	-

The RMSEs are measured with the method described in (Xiao et al. 2014). Bold text refers to *BEST AREA* and normal text refer to *BEST PRESSURE* models

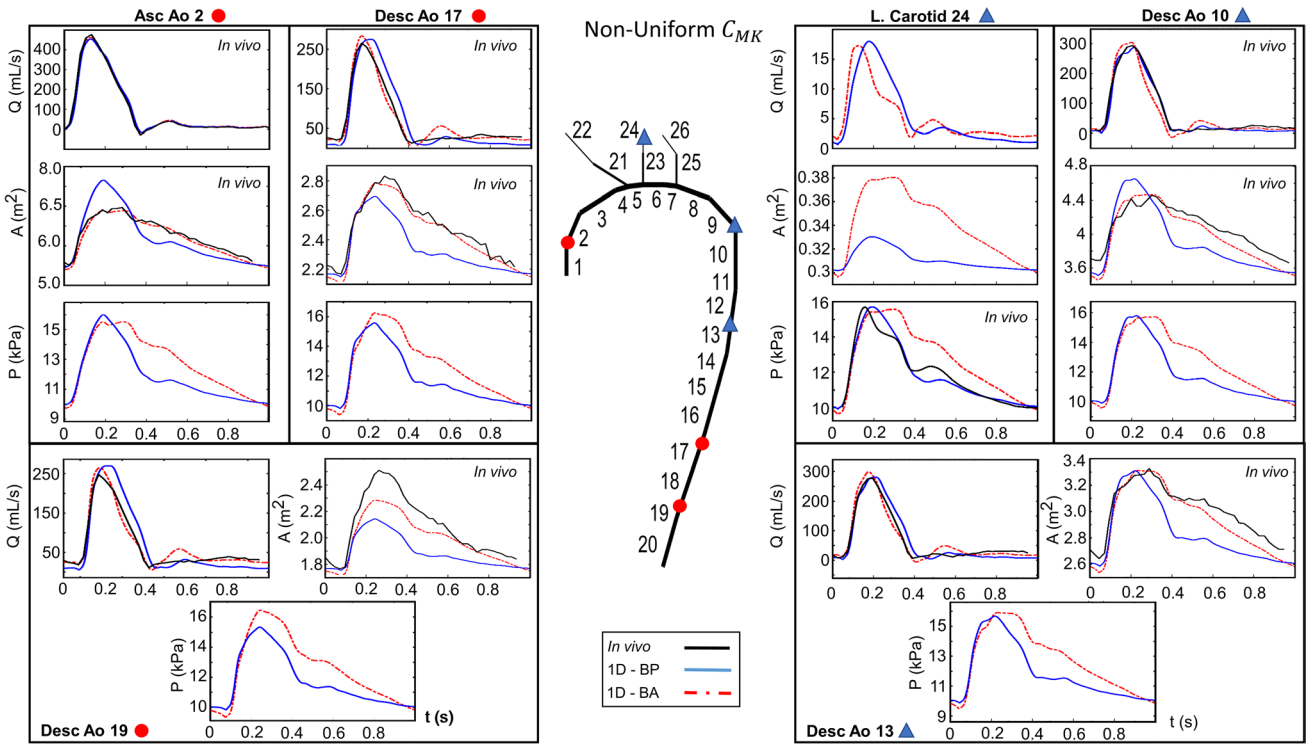

Fig. 9 Schematics and validation of the 26 segments model of arteries along the aorta and supra-aortic vessels with nonuniform speed of propagation. The model recreated in CardioFAN based on the same network presented in (Alastruey et al. 2016). Evaluated points on the left and right are specified on the schematics with red circles (segments 2-17-19) and blue triangles (segments 10-13-24), respectively. Pressure (P), flow (Q) and luminal area (A) plots show results of BEST AREA method (red dotted lines), BEST PRESSURE method (blue solid lines) and clinical in vivo measurements where available (black solid lines). Results are evaluated at the inlet of these segments, except for the common carotid artery, evaluated at the outlet of the segment (view the colored plots in online version)

artery, provides a good match with the clinically measured pressure at the same location and flow rates across all vessels; however, it under-predicts the luminal area as shown in Fig. 5. On the other hand, the *BEST AREA* case, prescribing the capillary pressure at the terminal boundaries, correctly predicts the luminal AREA in all locations, but it over-predicts the diastolic decay of the pressure at the common carotid artery. These results are in agreement with the 1D and 3D numerical predictions previously obtained by (Alastruey et al. 2016). Average relative errors of these predictions are shown in Table 2. The average relative errors for flow, luminal area and pressures, predicted with the corrected uniform C_{MK}, are smaller than 5.2%, 2.8% and 9% for *BEST AREA* and 7.6%, 7.1% and 1.6% for *BEST PRESSURE* cases (compared to 7%, 4% and 11% for BA and 9% 8% 4% for BP reported in (Alastruey et al. 2016)), respectively. We see an average of 1.5% improvement using the hyperelastic model with constant C_{MK}.

NonUniform $\boldsymbol{C_{MK}}$: flow, luminal area and pressure results for corrected nonuniform C_{mk} applied to each segment are shown in Fig. 9. Interested reader can refer to CardioFAN and run the nonuniform C_{MK} by changing the designated

parameter at the input and assigning the correctedC_{MK}. The compliance and resistances are corrected with the iterative method described by Xiao *et al.,* to correctly capture waveform range and diastolic pressure, respectively. The *BEST PRESSURE* case required no correction for R and C_j; however, for the *BEST AREA* case $R = 3.2 \times R_T$ and $C_j = C_j/2$ are used. We have applied the Fung constant $a = 4$, and $a = 8$, respectively, to account for hyperelastic properties, found iteratively by calibrating CardioFAN to the *in vivo* pressure data of the left carotid artery (*i.e*. segment 24).

Compared to (Alastruey et al. 2016), the results are demonstrating better prediction of flow rate (Q), luminal area (A) and pressure (P) using the TVD algorithm with hyperelastic vessel walls in both cases with uniform and nonuniform C_{MK} values. The nonuniform case C_{MK} shows a very good accuracy at predicting the luminal area peaks near systole. Accuracy can be further improved if the exact value of nonuniform C_{MK} (or its consequent elastic modulus) is known at each segment. With the current available measurements, the numerically calculated Q, A and P waveforms with uniform C_{MK} are more promising and therefore suggested for future studies.

4 Implications on the noninvasive diagnostics

The arterial pulse has historically been an essential source of information in the clinical assessment of health. Validation of the CardioFAN against prior numerical, *in vitro* and especially *in vivo* measurements combined with the improved method for PTT and PWV calculation, demonstrate reliability of the algorithm and its potential application to early patient-specific prediction/diagnostics of cardiovascular biomarkers. This algorithm can be used for noninvasive monitoring of the pressure, flow and luminal area waveforms, with minimal calibration of terminal resistance/compliances and Fung's constant a.

Due to the low-dispersive property, it will also be possible to use the TVD version of the code for calculating the pulse-wave propagation in the stented or prosthetic arteries, where discontinuous properties exist.

Further clinical studies with temporal pressure measurements available at all terminal boundaries are required to confidently suggest the reduced-order numerical techniques for clinical applications. Combined with noninvasive clinical measurements (*data assimilation* (Veneziani and Vergara 2013)) CardioFAN may provide patient-specific prediction of the central blood pressure, flow, stroke volume and arterial compliances.

5 Conclusion

We present a new monotonic TVD Lax–Wendroff-based platform for calculating patient-specific blood pressure, flow rate, luminal cross-sectional area and pulse transit time (PTT) inside an arbitrary cardiovascular network. This platform is free to use under the terms of the included open source license for CardioFAN. The variational formulation presented here and in our previous work makes this code ready to be coupled to 3D FSI modules to study 3D effects of diseases such as arterial aneurysms. Inlet and terminal boundary conditions are calculated based on minimal clinical or experimental calibration measurements, making it easy to run the model for patient-specific cases.

Three new validation tests are conducted here against numerical, as well as *in vitro* and *in vivo* data from three different geometries in the literature. These geometries and the vessel properties are prescribed in a demonstration version of CardioFAN, showing results of similar or improved errors compared to previous numerical simulators. We introduce a new numerical method for calculating the numerical PTT and use it in conjunction with experimental PTT to correct the speed of pulse propagation in arteries. This resulted in an average of 1.5% improvement in prediction of the clinically measured flow, luminal area and pressures. The corresponding average error of prediction is now smaller than 5.2%, 2.8% and 9% in *BEST AREA* and 7.6%, 7.1% and 1.6% for *BEST PRESSURE* simulation cases (refer to Sect. 3.4), respectively.

The reliability tests conducted here and the new method for calculating the corrected global PWV are building the groundworks for implementing CardioFAN as a means for noninvasive diagnostics of biomarkers. Further investigations can be focused on the reconstruction of patient-specific central pressure and flow (or stroke volume), using minimal peripheral measurements and calibration.

Acknowledgements The authors are grateful to Dr. Jordi Alastruey (Department of Biomedical Engineering, King's College London, London, UK) for providing us with the access to NEKTAR 1D algorithm, which allowed us to validate and improve CardioFAN, and both Dr. Jordi Alastruey and Dr. C. Alberto Figuera, for making their *in vivo* data for the aorta of a healthy patient available online.

Link to subject-specific data (Alastruey et al. 2016):
http://rsif.royalsocietypublishing.org/content/13/119/20160073

Funding This work was supported by a start-up grant from Rochester Institute of Technology (RIT) to establish "Laboratory of Applied Nonlinear Mechanics (LANMech)".

Compliance with ethical standards

Conflicts of interest The authors declare that they have no conflict of interest.

Appendix A

Lax–Wendroff Method:

Nonlinear conservation equations listed in Eq. (17) can be rearranged as follows

$$\frac{\partial \boldsymbol{Q}}{\partial t} = \boldsymbol{f} - \frac{\partial \boldsymbol{F}(\boldsymbol{Q})}{\partial x}; \tag{A1}$$

Jacobian matrices of vector functions $\boldsymbol{F}_{\boldsymbol{Q}} = \frac{\partial \boldsymbol{F}}{\partial \boldsymbol{Q}}, \boldsymbol{f}_{\boldsymbol{Q}} = \frac{\partial \boldsymbol{f}}{\partial \boldsymbol{Q}}$ of Eq. (17) are

$$\boldsymbol{F}_{\boldsymbol{Q}} = \boldsymbol{H} = \begin{bmatrix} V & A \\ \frac{P_A}{\rho} & V \end{bmatrix}, \quad \boldsymbol{f}_{\boldsymbol{Q}} = \frac{k}{A}\begin{bmatrix} 0 & 0 \\ -\frac{V}{A} & 1 \end{bmatrix} \tag{A2}$$

A detailed discretization based on Lax–Wendroff scheme is previously shown in (Vahedein and Liberson 2018b). Following notation typical for finite volume methods (as shown by (LeVeque 2002)), here the space domain is discretized with uniformly distributed cells, whose center points are indicated by a low integer index j, and the edge points are noted by fractional indices $j \pm \frac{1}{2}$. Associating flux functions with the cell edges we get the Lax–Wendroff-based discretized solution

$$\begin{aligned} \boldsymbol{Q}_j^{n+1} &= \boldsymbol{Q}_j^n - \frac{\Delta t}{\Delta x}(\boldsymbol{F}^n_{j+\frac{1}{2}} - \boldsymbol{F}^n_{j-\frac{1}{2}}) + \boldsymbol{Q}^n_{fj} \\ \boldsymbol{F}^n_{j+\frac{1}{2}} &= \frac{\boldsymbol{F}^n_j + \boldsymbol{F}^n_{j+1}}{2} - \frac{\Delta t}{2\Delta x}\boldsymbol{H}^n_{\frac{j+1}{2}}\left(\boldsymbol{F}^n_{j+1} - \boldsymbol{F}^n_j\right) \end{aligned} \tag{A3}$$

$$\begin{aligned} \boldsymbol{Q}^n_{fj} &= \Delta t f^n \\ &+ \frac{\Delta t^2}{2}\left[\boldsymbol{f}_{\boldsymbol{Q}}\left(\boldsymbol{f} - \frac{\partial \boldsymbol{F}(\boldsymbol{Q})}{\partial x}\right) - \frac{\partial}{\partial x}(\boldsymbol{F}_{\boldsymbol{Q}}\boldsymbol{f})\right]^n \end{aligned}$$

where n refers to the current time step, and Δt is the time step. The convergence criteria for the Lax–Wendroff scheme is defined by Courant–Friedrichs–Lewy (CFL) condition

$$CFL = \frac{\tau(V + c_{MK})_{max}}{\Delta x} \leq 1 \tag{A4}$$

High-Resolution Lax–Wendroff Scheme (TVD Method):

As shown in (LeVeque 2002), the dispersive nature of all non-monotone methods, including Lax–Wendroff, causes artificial oscillations in the vicinity of discontinuities. The idea behind high-resolution schemes is in introduction of the flux limiters, that correct the flux terms depending on the local solution behavior, retaining monotonicity in case of a discontinuity.

Following Leveque, we present fluxes in a form revealing explicitly diffusive flux components $\tilde{F}_{j+\frac{1}{2}}$ (upper index dropped for simplicity)

$$\begin{aligned} \boldsymbol{F}_{j+\frac{1}{2}} &= \frac{1}{2}\left[\boldsymbol{F}_j + \boldsymbol{F}_{j+1} - \left|\boldsymbol{H}_{j+\frac{1}{2}}\right|\boldsymbol{\Delta Q}_{j+\frac{1}{2}}\right] + \widetilde{\boldsymbol{F}}_{j+\frac{1}{2}} \\ \widetilde{\boldsymbol{F}}_{j+\frac{1}{2}} &= \frac{1}{2}\boldsymbol{R}_{j+\frac{1}{2}}\left|\boldsymbol{\Lambda}_{j+\frac{1}{2}}\right|\left(\boldsymbol{I} - \frac{\Delta t}{\Delta x}\left|\boldsymbol{\Lambda}_{j+\frac{1}{2}}\right|\right)\boldsymbol{\Delta W}_{j+\frac{1}{2}} \end{aligned} \tag{A5}$$

$$\begin{aligned} \boldsymbol{H}_{j+\frac{1}{2}} &= \boldsymbol{R}_{j+\frac{1}{2}}\,\boldsymbol{\Lambda}_{j+\frac{1}{2}}\,\boldsymbol{R}^{-1}_{j+\frac{1}{2}}; \\ \boldsymbol{\Delta Q}_{j+\frac{1}{2}} &= \boldsymbol{Q}_{j+1} - \boldsymbol{Q}_j; \\ \boldsymbol{\Delta W}_{j+\frac{1}{2}} &= \boldsymbol{R}^{-1}_{j+\frac{1}{2}}\boldsymbol{\Delta Q}_{j+\frac{1}{2}}; \end{aligned} \tag{A6}$$

where I - identity matrix, $\boldsymbol{R}_{j+\frac{1}{2}}$, $\boldsymbol{\Lambda}_{j+\frac{1}{2}}$ – are the modal and eigenvalue matrices of Jacobian matrix $H_{j+\frac{1}{2}}$. The correction flux, satisfying to the monotonicity conditions is based on a substitution of the eigenvector increment $\boldsymbol{\Delta W}_{j+\frac{1}{2}}$ by its limited version $\boldsymbol{\Delta}\tilde{\boldsymbol{W}}_{j+\frac{1}{2}}$ (LeVeque 2002)

$$\begin{aligned} &\boldsymbol{\Delta}\widetilde{\boldsymbol{W}}_{j+\frac{1}{2}} = \psi\left(r_{j+\frac{1}{2}}\right)\Delta \boldsymbol{W}_{j+\frac{1}{2}}, \qquad r_{j+\frac{1}{2}} = \frac{\boldsymbol{W}_{j+1} - \boldsymbol{W}_j}{\boldsymbol{W}_j - \boldsymbol{W}_{j-1}}, \\ &\psi = max[0, min(2r, 1),\ min(r, 2)] \qquad < ex. \quad Superbee > \end{aligned} \tag{A7}$$

Appendix B

Exact Manufactured Solution for Linear Wave in Stented Artery): A closed-form solution for the harmonic linear wave analysis is derived for the case of a stented artery depicted in Fig. 2. Alternatively, the system (17) can be recast in terms of conserved variables: the total pressure $P_0 = p + \frac{1}{2}\rho V^2$and a flow rate $q = AV$

$$\frac{\partial}{\partial t}\begin{Bmatrix} A \\ q/A \end{Bmatrix} + \frac{\partial}{\partial x}\begin{Bmatrix} q \\ P_0/\rho \end{Bmatrix} = 0 \tag{B1}$$

A linear elastic tube law complements the system (B1) in the form of the following pressure – area relationship

$$P = 2\rho_f c^2_{mk}\left(\sqrt{\frac{A}{A_0}} - 1\right) \tag{B2}$$

The linearization around zero point for transmural pressure and the flow rate reads

$$\frac{\partial}{\partial t}\begin{Bmatrix} A \\ q \end{Bmatrix} + \frac{\partial}{\partial x}\begin{Bmatrix} q \\ \frac{A_0}{\rho_f}p \end{Bmatrix} = 0 \tag{B3}$$

$$p = \rho_f c^2_{mk}\left(\frac{A}{A_0} - 1\right) \tag{B4}$$

To eliminate cross-sectional area A we substitute Eq. (B4) into Eq. (B3), recasting final system of equations in terms of conserved variables $(p,\ q)$

$$\frac{\partial}{\partial t}\begin{Bmatrix} p \\ q \end{Bmatrix} + \frac{\partial}{\partial x}\begin{Bmatrix} \frac{\rho_f c_{mk}^2}{A_0} q \\ \frac{A_0}{\rho_f} p \end{Bmatrix} = 0 \tag{B5}$$

An explicit closed-form solution has been manufactured in the form of a single harmonic wave satisfying Eq. (B5) for each segment

$$\begin{aligned} q_i(x_i,t) &= (1+\sin(\omega t)) \\ &\left[C_{1i}\cos\left(\frac{\omega x_i}{c_{MK,i}}\right)+C_{2i}\sin\left(\frac{\omega x_i}{c_{MK,i}}\right)\right] \\ p_i(x_i,t) &= \overline{p}+\frac{\rho_f c_{MK,i}}{A_0}\cos(\omega t) \\ &\left[-C_{1i}\sin\left(\frac{\omega x_i}{c_{MK,i}}\right)+C_{2i}\cos\left(\frac{\omega x_i}{c_{MK,i}}\right)\right] \end{aligned} \tag{B6}$$

Here, $q_i(x_i)$, $p_i(x_i)$ are the flow rate and pressure distributions for each segment as functions of a local axial coordinate x_i (Fig. 2); ω is the frequency of the harmonic wave; $c_{MK,i}$ is the Moens-Korteweg speed of propagation for each segment, $i = 1,\ 2,\ 3$ (corresponding to artery, stent and artery configuration in Fig. 2). Six unknown constants C_{1i}, C_{2i} satisfy to the inlet boundary conditions for the flow rate

$$q_1(x_1 = 0,\ t) = (1+\sin(\omega t)\ )Q_0 \tag{B7}$$

exit boundary condition for the pressure

$$p_3(x_3 = L_3, t) = \overline{p} + \cos(\omega t)\, p_a \tag{B8}$$

and four matching conditions at each interface

$$\begin{aligned} q_1(x_1 = L_1, t) &= q_2(x_2 = 0, t) \\ p_1(x_1 = L_1, t) &= p_2(x_2 = 0, t) \\ q_2(x_2 = L_2, t) &= q_3(x_3 = 0, t) \\ p_2(x_2 = L_2, t) &= p_3(x_3 = 0, t). \end{aligned} \tag{B9}$$

References

Alastruey JA (2006) Numerical modelling of pulse wave propagation in the cardiovascular system : development, validation and clinical applications. PhD thesis, University of London

Alastruey J, Parker KH, Sherwin SJ (2008) Lumped parameter outflow models for 1-D blood flow simulations: Effect on pulse waves and parameter estimation. Commun Comput Phys

Alastruey J, Khir AW, Matthys KS, Segers P, Sherwin SJ, Verdonck PR, Parker KH, Peiró J (2011) Pulse wave propagation in a model human arterial network: assessment of 1-D visco-elastic simulations against in vitro measurements. J Biomech 44(12):2250–2258. https://doi.org/10.1016/j.jbiomech.2011.05.041

Alastruey J, Parker KH, Sherwin SJ (2012) Arterial pulse wave haemodynamics. In: Anderson S (ed) 11th international conference on pressure surges, Virtual PiE Led t/a BHR Group, pp 401–443

Alastruey J, Xiao N, Fok H, Schaeffter T, Figueroa CA (2016) On the impact of modelling assumptions in multi-scale, subject-specific models of aortic haemodynamics. J R Soc Interface 13(119):20160073. https://doi.org/10.1098/rsif.2016.0073

Anliker M, Rockwell RL, Ogden E (1970) Nonlinear analysis of flow pulses and shock waves in arteries. Zeitschrift für angewandte Mathematik und Physik ZAMP 22(2):217–246. https://doi.org/10.1007/BF01591407

Back M, Kopchok G, Mueller M, Cavaye D, Donayre C, White RA (1994) Changes in arterial wall compliance after endovascular stenting. J Vasc Surg 19(5):905–911. https://doi.org/10.1016/S0741-5214(94)70017-6

Berdichevsky VL (2009) Variational principles. In: Variational principles of continuum mechanics, interaction of mechanics and mathematics, Springer Berlin Heidelberg, pp 3–44, https://doi.org/10.1007/978-3-540-88467-5_1

Bergel DH (1961) The dynamic elastic properties of the arterial wall. Journal Physiol 156(3):458–469

Bronzino J (2005) 1 - Biomedical engineering: a historical perspective. In: Enderle JD, Blanchard SM, Bronzino JD (eds) Introduction to Biomedical Engineering (Second Edition), Academic Press, Boston, pp 1–29, https://doi.org/10.1016/B978-0-12-238662-6.50003-3

Carek AM, Conant J, Joshi A, Kang H, Inan OT (2017) SeismoWatch: wearable cuffless blood pressure monitoring using pulse transit time. Proc ACM Interact Mob Wearable Ubiquitous Technol 1(3):40:1–40:16, https://doi.org/10.1145/3130905

Caro CG, Pedley TJ, Schroter RC, Seed WA (2011) Mech Circ, 2nd edn. Cambridge University Press, Cambridge

Chapra SC, Canale RP (1997) Numer Methods Eng Program Softw Appl, 3rd edn. McGraw-Hill Inc, New York

Djelić M, Mazić S, Žikić D (2013) A novel laboratory approach for the demonstration of hemodynamic principles: the arterial blood flow reflection. Adv Physiol Edu 37(4):321–326. https://doi.org/10.1152/advan.00176.2012

Dong S, Insley J, Karonis NT, Papka ME, Binns J, Karniadakis G (2006) Simulating and visualizing the human arterial system on the teragrid. Future Gener Comput Syst 22(8):1011–1017. https://doi.org/10.1016/j.future.2006.03.019

Dúóng M, Nguyen N, Staat M (2017) Physical response of hyperelastic models for composite materials and soft tissues

Figueroa CA, Baek S, Taylor CA, Humphrey JD (2009) A computational framework for fluid-solid-growth modeling in cardiovascular simulations. Comput Methods Appl Mech Eng 198(45–46):3583–3602. https://doi.org/10.1016/j.cma.2008.09.013

Foo JYA, Lim CS (2006) Pulse transit time as an indirect marker for variations in cardiovascular related reactivity. Technol Health Care Off J Eur Soc Eng Med 14(2):97–108

Formaggia L, Lamponi D, Quarteroni A (2003) One-dimensional models for blood flow in arteries. J Eng Math 47(3–4):251–276. https://doi.org/10.1023/B:ENGI.0000007980.01347.29

Funamoto K, Hayase T (2012) Reproduction of pressure field in ultrasonic-measurement-integrated simulation of blood flow. Int J Numer Methods Biomed Eng 29(7):726–740. https://doi.org/10.1002/cnm.2522

Fung YC, Fronek K, Patitucci P (1979) Pseudoelasticity of arteries and the choice of its mathematical expression. Am J Physiol 237(5):H620–631

Gaddum NR, Alastruey J, Beerbaum P, Chowienczyk P, Schaeffter T (2013) A technical assessment of pulse wave velocity algorithms applied to non-invasive arterial waveforms. Ann Biomed Eng 41(12):2617–2629. https://doi.org/10.1007/s10439-013-0854-y

García G, Teresa M, Acevedo T, Fernanda M, Rodriguez Guzmán M, Alegre de Montaner R, Fernández Fernández B, del Río Camacho G, González-Mangado N (2014) Can pulse transit time be useful for detecting hypertension in patients in a sleep unit? Archivos de Bronconeumología (English Edition) 50(7):278–284. https://doi.org/10.1016/j.arbr.2014.05.001

Ghigo A, Wang XF, Armentano R, Lagrée PY, Fullana JM (2016) Linear and nonlinear viscoelastic arterial wall models: application on animals. arXiv:160707973 [physics] 1607.07973

Gray RA, Pathmanathan P (2018) Patient-specific cardiovascular computational modeling: diversity of personalization and challenges. Journal of Cardiovascular Translational Research pp 1–9, https://doi.org/10.1007/s12265-018-9792-2

Grinberg L, Karniadakis GE (2008) Outflow boundary conditions for arterial networks with multiple outlets. Ann Biomed Eng 36(9):1496–1514. https://doi.org/10.1007/s10439-008-9527-7

Harten A (1983) High resolution schemes for hyperbolic conservation laws. J Comput Phys 49(3):357–393. https://doi.org/10.1016/0021-9991(83)90136-5

Humphrey J, Taylor C (2008) Intracranial and abdominal aortic aneurysms: similarities, differences, and need for a new class of computational models. annual review of biomedical engineering 10:221–246. DOI 10.1146/annurev.bioeng.10.061807.160439

Humphrey JD (1995) Mechanics of the arterial wall: review and directions. Crit Rev Biomed Eng 23(1–2):1–162

Itu LM, Sharma P, Suciu C (eds) (2017) Patient-specific hemodynamic computations: application to personalized diagnosis of cardiovascular pathologies. Springer International Publishing

Kolodgie FD, Nakazawa G, Sangiorgi G, Ladich E, Burke AP, Virmani R (2007) Pathology of Atherosclerosis and Stenting. Neuroimaging clinics of North America 17(3):285–vii. https://doi.org/10.1016/j.nic.2007.03.006

LeVeque RJ (2002) Finite volume methods for hyperbolic problems. Cambridge Texts in Applied Mathematics, Cambridge University Press, Cambridge, https://doi.org/10.1017/CBO9780511791253

Liang F, Guan D, Alastruey J (2018) Determinant factors for arterial hemodynamics in hypertension: theoretical insights from a computational model-based study. J Biomech Eng 140(3):031006–031006–14, https://doi.org/10.1115/1.4038430

Liberson AS, Lillie JS, Day SW, Borkholder DA (2016) A physics based approach to the pulse wave velocity prediction in compliant arterial segments. J Biomech 49(14):3460–3466. https://doi.org/10.1016/j.jbiomech.2016.09.013

Liberson AS, Vahedein YS, Borkholder DA (2017) Application of variational principle to form reduced fluid-structure interaction models in bifurcated. J Fluid Flow, Heat and Mass Transf (JFFHMT) 4(1):1–9

Lillie JS, Liberson AS, Borkholder DA (2016) Improved blood pressure prediction using systolic flow correction of pulse wave velocity. Cardiovasc Eng Technol 7(4):439–447. https://doi.org/10.1007/s13239-016-0281-y

Matthys KS, Alastruey J, Peiró J, Khir AW, Segers P, Verdonck PR, Parker KH, Sherwin SJ (2007) Pulse wave propagation in a model human arterial network: assessment of 1-D numerical simulations against in vitro measurements. J Biomech 40(15):3476–3486. https://doi.org/10.1016/j.jbiomech.2007.05.027

McEniery CM, Yasmin n, McDonnell B, Munnery M, Wallace SM, Rowe CV, Cockcroft JR, Wilkinson IB, Anglo-cardiff collaborative trial investigators (2008) central pressure: variability and impact of cardiovascular risk factors: The Anglo-Cardiff Collaborative Trial II. Hypertension (Dallas, Tex: 1979) 51(6):1476–1482, https://doi.org/10.1161/HYPERTENSIONAHA.107.105445

McEniery CM, Cockcroft JR, Roman MJ, Franklin SS, Wilkinson IB (2014) Central blood pressure: current evidence and clinical importance. Eur Heart J 35(26):1719–1725. https://doi.org/10.1093/eurheartj/eht565

Mitchell GF (2009) Arterial stiffness and wave reflection: biomarkers of cardiovascular risk. Artery Res 3(2):56–64. https://doi.org/10.1016/j.artres.2009.02.002

Mukkamala R, Hahn JO, Inan OT, Mestha LK, Kim CS, Töreyin H, Kyal S (2015) Toward ubiquitous blood pressure monitoring via pulse transit time: theory and practice. IEEE Trans Bio-med Eng 62(8):1879–1901. https://doi.org/10.1109/TBME.2015.2441951

Mungkasi S, Ningrum GIJ (2016) Numerical solution to the linear acoustics equations. In: AIP conference proceedings 1746(1):020056. https://doi.org/10.1063/1.4953981

Nelson MR, Stepanek J, Cevette M, Covalciuc M, Hurst RT, Tajik AJ (2010) Noninvasive measurement of central vascular pressures with arterial tonometry: Clinical revival of the pulse pressure waveform? Mayo Clin Proc 85(5):460–472. https://doi.org/10.4065/mcp.2009.0336

Nichols WW, Edwards DG (2001) Arterial elastance and wave reflection augmentation of systolic blood pressure: deleterious effects and implications for therapy. J Cardiovasc Pharmacol Ther 6(1):5–21. https://doi.org/10.1177/107424840100600102

Obeid H, Soulat G, Mousseaux E, Laurent S, Stergiopulos N, Boutouyrie Pierre, Segers P (2017) Numerical assessment and comparison of pulse wave velocity methods aiming at measuring aortic stiffness. Physiol Meas 38(11):1953. https://doi.org/10.1088/1361-6579/aa905a

Olufsen MS, Peskin CS, Kim WY, Pedersen EM, Nadim A, Larsen J (2000) Numerical simulation and experimental validation of blood flow in arteries with structured-tree outflow conditions. Ann Biomed Eng 28(11):1281–1299. https://doi.org/10.1114/1.1326031

Parazynski SE, Tucker BJ, Aratow M, Crenshaw A, Hargens AR (1993) Direct measurement of capillary blood pressure in the human lip. Journal of Applied Physiology (Bethesda, Md: 1985) 74(2):946–950, https://doi.org/10.1152/jappl.1993.74.2.946

Parkhurst KL, Lin HF, DeVan AE, Barnes JN, Tarumi T, Tanaka H (2012) Contribution of blood viscosity in the assessment of flow-mediated dilation and arterial stiffness. Vasc Med 17(4):231–234. https://doi.org/10.1177/1358863X12450095

Peiró J, Veneziani A (2009) Reduced models of the cardiovascular system. In: Formaggia L, Quarteroni A, Veneziani A (eds) Cardiovascular mathematics: modeling and simulation of the circulatory system, MS&A, Springer Milan, Milano, pp 347–394, https://doi.org/10.1007/978-88-470-1152-6_10

Pereira T, Correia C, Ja Cardoso (2015) Novel methods for pulse wave velocity measurement. J Med Biol Eng 35(5):555–565. https://doi.org/10.1007/s40846-015-0086-8

Perktold K, Resch M, Peter RO (1991) Three-dimensional numerical analysis of pulsatile flow and wall shear stress in the carotid artery bifurcation. J Biomech 24(6):409–420. https://doi.org/10.1016/0021-9290(91)90029-M

Poleszczuk J, Debowska M, Dabrowski W, Wojcik-Zaluska A, Zaluska W, Waniewski J (2018) Subject-specific pulse wave propagation modeling: towards enhancement of cardiovascular assessment methods. PLOS ONE 13(1):e0190972. https://doi.org/10.1371/journal.pone.0190972

Pries AR, Neuhaus D, Gaehtgens P (1992) Blood viscosity in tube flow: dependence on diameter and hematocrit. Am J Physiol Heart Circ Physiol 263(6):H1770–H1778

Rabben SI, Stergiopulos N, Hellevik LR, Smiseth OA, Slørdahl S, Urheim S, Angelsen B (2004) An ultrasound-based method for determining pulse wave velocity in superficial arteries. J Biomech 37(10):1615–1622. https://doi.org/10.1016/j.jbiomech.2003.12.031

Reule S, Drawz PE (2012) Heart rate and blood pressure: Any possible implications for management of hypertension? Curr

Hypertens Rep 14(6):478–484. https://doi.org/10.1007/s11906-012-0306-3
Reymond P, Merenda F, Perren F, Rüfenacht D, Stergiopulos N (2009) Validation of a one-dimensional model of the systemic arterial tree. Am J Physiol Heart Circ Physiol 297(1):H208–H222. https://doi.org/10.1152/ajpheart.00037.2009
Roe PL (1984) Generalized formulation of TVD Lax–Wendroff schemes. Tech. rep
Sankar DS, Hemalatha K (2007) A non-Newtonian fluid flow model for blood flow through a catheterized artery—Steady flow. Appl Math Model 31(9):1847–1864. https://doi.org/10.1016/j.apm.2006.06.009
Schultz DL, Tunstall-Pedoe DS, Lee GdJ, Gunning AJ, Bellhouse BJ (2008) Velocity distribution and transition in the arterial system. In: Ciba foundation symposium - circulatory and respiratory mass transport, Wiley-Blackwell, pp 172–202, https://doi.org/10.1002/9780470719671.ch11
Segers P, Rietzschel ER, Buyzere MLD, Vermeersch SJ, Bacquer DD, Bortel LMV, Backer GD, Gillebert TC, Verdonck PR (2007) Noninvasive (Input) Impedance, Pulse Wave Velocity, and Wave Reflection in Healthy Middle-Aged Men and Women. Hypertension 49(6):1248–1255. https://doi.org/10.1161/HYPERTENSIONAHA.106.085480
Sharman JE, Stowasser M, Fassett RG, Marwick TH, Franklin SS (2008) Central blood pressure measurement may improve risk stratification. J Hum Hypertens 22(12):838–844. https://doi.org/10.1038/jhh.2008.71
Sharwood-Smith G, Bruce J, Drummond G (2006) Assessment of pulse transit time to indicate cardiovascular changes during obstetric spinal anaesthesia. BJA Br J Anaesth 96(1):100–105. https://doi.org/10.1093/bja/aei266
Sherwin SJ, Formaggia L, Peiró J, Franke V (2003a) Computational modelling of 1D blood flow with variable mechanical properties and its application to the simulation of wave propagation in the human arterial system. Int J Numer Methods Fluids 43(6–7):673–700. https://doi.org/10.1002/fld.543
Sherwin SJ, Franke V, Peiró J, Parker K (2003b) One-dimensional modelling of a vascular network in space-time variables. J Eng Math 47(3–4):217–250. https://doi.org/10.1023/B:ENGI.0000007979.32871.e2
Shi Y, Lawford P, Hose R (2011) Review of zero-D and 1-D models of blood flow in the cardiovascular system. BioMed Eng OnLine 10:33. https://doi.org/10.1186/1475-925X-10-33
Smith N, Pullan A, Hunter P (2002) An anatomically based model of transient coronary blood flow in the heart. SIAM J Appl Math 62(3):990–1018. https://doi.org/10.1137/S0036139999355199
Tavallali P, Razavi M, Pahlevan NM (2018) Artificial intelligence estimation of carotid-femoral pulse wave velocity using carotid waveform. Scientific Reports 8, https://doi.org/10.1038/s41598-018-19457-0
Trachet B, Reymond P, Kips J, Swillens A, De Buyzere M, Suys B, Stergiopulos N, Segers P (2010) Numerical validation of a new method to assess aortic pulse wave velocity from a single recording of a brachial artery waveform with an occluding cuff. Ann Biomed Eng 38(3):876–888. https://doi.org/10.1007/s10439-010-9945-1
Tortoriello A, Pedrizzetti G (2004) Flow-tissue interaction with compliance mismatch in a model stented artery. J Biomech 37:1–11
Vahedein YS, Liberson AS (2017) Reduced modeling framework of circulatory system revisited. In: International conference of fluid Flow, heat and mass transfer, https://doi.org/10.11159/ffhmt17.174
Vahedein YS, Liberson AS (2018a) Validation and application of a physically nonlinear id computational model for bifurcated arterial networks*. In: 2018 40th Annual international conference of the ieee engineering in medicine and biology society (EMBC), pp 5253–5256, https://doi.org/10.1109/EMBC.2018.8513448
Vahedein YS, Liberson AS (2018b) Validation of a multi-branched patient specific computational model for human arterial systems. In: International conference of fluid flow, heat and mass transfer, https://doi.org/10.11159/ffhmt18.156
Vahedein S, Yashar Karnam Y, Liberson AS (2018) Predictive multiscale approach (3D–1D) for blood flow simulations in cardiovascular networks. IEEE Eng Med Biol (EMBC) 2018:1
van Bakel TMJ, Lau KD, Hirsch-Romano J, Trimarchi S, Dorfman AL, Figueroa CA (2018) Patient-specific modeling of hemodynamics: supporting surgical planning in a fontan circulation correction. J Cardiovasc Trans Res pp 1–11, https://doi.org/10.1007/s12265-017-9781-x
van de Vosse FN, Stergiopulos N (2011) Pulse wave propagation in the arterial tree. Annu Rev Fluid Mech 43(1):467–499. https://doi.org/10.1146/annurev-fluid-122109-160730
Veneziani A, Vergara C (2013) Inverse problems in Cardiovascular mathematics: toward patient-specific data assimilation and optimization. Int J Numer Methods Biomed Eng 29(7):723–725. https://doi.org/10.1002/cnm.2566
Vennin S, Mayer A, Li Y, Fok H, Clapp B, Alastruey J, Chowienczyk P (2015) Noninvasive calculation of the aortic blood pressure waveform from the flow velocity waveform: a proof of concept. Am J Physiol Heart Circ Physiol 309(5):H969–H976. https://doi.org/10.1152/ajpheart.00152.2015
Westerhof N, Elzinga G, Sipkema P (1971) An artificial arterial system for pumping hearts. J Appl Physiol 31(5):776–781
Willemet M, Lacroix V, Marchandise E (2011) Inlet boundary conditions for blood flow simulations in truncated arterial networks. J Biomech 44(5):897–903. https://doi.org/10.1016/j.jbiomech.2010.11.036
Xiao N, Alastruey J, Figueroa CA (2014) A systematic comparison between 1-D and 3-D hemodynamics in compliant arterial models. Int J Numer Methods Biomed Eng 30(2):204–231. https://doi.org/10.1002/cnm.2598